PERGAMON

Available online at www.sciencedirect.com

SCIENCE @ DIRECT®

Progress in Aerospace Sciences 39 (2003) 329–367

PROGRESS IN AEROSPACE SCIENCES

www.elsevier.com/locate/paerosci

Viscous flow computations with the method of lattice Boltzmann equation

Dazhi Yu[a], Renwei Mei[a,]*, Li-Shi Luo[b,1], Wei Shyy[a]

[a] *Department of Mechanical and Aerospace Engineering, University of Florida, 231 Aerospace Building P.O. Box 116250, Gainesville, FL 32611-6250, USA*

[b] *ICASE, MS 132C, NASA Langley Research Center, 3 West Reid Street, Building 1152, Hampton, Virginia 23681-2199, USA*

Abstract

The method of lattice Boltzmann equation (LBE) is a kinetic-based approach for fluid flow computations. This method has been successfully applied to the multi-phase and multi-component flows. To extend the application of LBE to high Reynolds number incompressible flows, some critical issues need to be addressed, noticeably flexible spatial resolution, boundary treatments for curved solid wall, dispersion and mode of relaxation, and turbulence model. Recent developments in these aspects are highlighted in this paper. These efforts include the study of force evaluation methods, the development of multi-block methods which provide a means to satisfy different resolution requirement in the near wall region and the far field and reduce the memory requirement and computational time, the progress in constructing the second-order boundary condition for curved solid wall, and the analyses of the single-relaxation-time and multiple-relaxation-time models in LBE. These efforts have lead to successful applications of the LBE method to the simulation of incompressible laminar flows and demonstrated the potential of applying the LBE method to higher Reynolds flows. The progress in developing thermal and compressible LBE models and the applications of LBE method in multi-phase flows, multi-component flows, particulate suspensions, turbulent flow, and micro-flows are reviewed.

Keywords: Lattice Boltzmann equation; Force evaluation; Grid refinement; Multi-block; Boundary condition; Single-relaxation-time; Multi-relaxation-time

---

Contents

---

*Corresponding author. Tel.: +1-352-392-0888; fax: +1-352-392-7303.

E-mail address: rwm@mae.ufl.edu (R. Mei).

[1] Current address: National Institute of Aerospace, 144 Research Drive, Hampton, Virginia 23666 USA.

0376-0421/03/$ - see front matter © 2003 Published by Elsevier Science Ltd.
doi:10.1016/S0376-0421(03)00003-4

Nomenclature

f	single particle mass distribution function
$\boldsymbol{\xi}$	particle velocity vector
$\boldsymbol{u}$	fluid velocity
p	pressure
$\boldsymbol{x}$	spatial position vector
$f^{(0)}$	equilibrium distribution function
$\tilde{f}_\alpha$	post-collision distribution function
λ	relaxation time
R	gas constant
T	gas temperature
v	kinematic viscosity
$\boldsymbol{e}_\alpha$	discrete particle velocity in LBE model
w_α	weighting factor
$f_\alpha^{(\mathrm{eq})}$	equilibrium distribution function in discretized particle velocity space
$f_\alpha^{(\mathrm{neq})}$	non-equilibrium distribution function in discretized particle velocity space
c_s	speed of sound.
δt	time step
δx	space step
τ	dimensionless relaxation time in LBGK
$\boldsymbol{x}_\mathrm{f}$	lattice node on the fluid side next to the boundary
$\boldsymbol{x}_\mathrm{b}$	lattice node on the solid side next to the boundary
$\boldsymbol{x}_\mathrm{w}$	intersection of the wall with lattice link
$\boldsymbol{u}_\mathrm{w}$	wall velocity
Δ	$\lvert x_\mathrm{f} - x_\mathrm{w}\rvert / \lvert x_\mathrm{f} - x_\mathrm{b}\rvert$
e	energy
ε	a variable related to the square of the energy
j_x, j_y	mass flux
q_x, q_y	variables corresponding to the energy flux
p_{xx}, p_{xy}	variables corresponding to the diagonal and off-diagonal components of the viscous stress tensor
$\tilde{f}_\alpha$	denotes the post-collision state
C_D	drag coefficient
C_L	lift coefficient

Abbreviations

BGK	Bhatnagar–Gross–Krook
CFD	computational fluid dynamics
CFL	Courant–Friedrichs–Lewy
DVM	discrete velocity model
D2Q9	2-D 9-velocity
LBE	lattice Boltzmann equation
LBGK	lattice BGK
LES	large-eddy simulation
LGA	lattice gas automata
MRT	multi-relaxation-time
NS	Navier–Stokes
PDE	partial differential equation
SRT	single-relaxation-time
TLBE	thermal lattice Boltzmann equation

1. Introduction

1.1. Method of lattice Boltzmann equation

In the last 15 years or so, there has been rapid progress in developing the method of the lattice Boltzmann equation (LBE) for solving a variety of fluid dynamic problems [1–17]. Historically, the LBE method was developed from the method of lattice gas automata (LGA); see [18–22] for details on LGA method. Nevertheless, the LBE method can be better appreciated by considering the Boltzmann equation directly. Adopting the macroscopic method for computational fluid dynamics (CFD), the macroscopic variables of interest, such as velocity $\boldsymbol{u}$ and pressure p, are usually obtained by solving the Navier–Stokes (NS) equations (e.g., [23,24]). In the LBE approach, one solves the kinetic equation for the particle velocity distribution function $f(\boldsymbol{x}, \boldsymbol{\xi}, t)$ in which $\boldsymbol{\xi}$ is the particle velocity vector, $\boldsymbol{x}$ is the spatial position vector, and t is the time. The macroscopic quantities (such as mass density ρ and momentum density $\rho\boldsymbol{u}$) can then be obtained by evaluating the hydrodynamic moments of the distribution function f. This approach was first proposed by McNamara and Zanetti [25], with the additional theoretical foundation established in the subsequent papers, notably, Higuera and Jiménez [26], Koelman [27], Qian et al. [28], Chen et al. [29], and d'Humières [30].

A popular kinetic model adopted in the literature is the single-relaxation-time (SRT) approximation, the so-called Bhatnagar–Gross–Krook (BGK) model [31]:

$$\frac{\partial f}{\partial t} + \boldsymbol{\xi} \cdot \nabla f = -\frac{1}{\lambda}(f - f^{(0)}), \tag{1}$$

where $f^{(0)}$ is the equilibrium distribution function (the Maxwell–Boltzmann distribution function), and λ is the relaxation time. The corresponding viscosity is $\upsilon = \lambda RT$ in which R is the gas constant and T is the gas temperature.

To solve for f numerically, Eq. (1) is first discretized in the velocity space using a finite set of velocity vectors $\{\boldsymbol{\xi}_\alpha\}$ in the context of the conservation laws [32,33]:

$$\frac{\partial f_\alpha}{\partial t} + \boldsymbol{\xi}_\alpha \cdot \nabla f_\alpha = -\frac{1}{\lambda}(f_\alpha - f_\alpha^{(\text{eq})}). \tag{2}$$

In the above equation, $f_\alpha(\boldsymbol{x}, t) \equiv f(\boldsymbol{x}, \xi_\alpha, t)$ is the distribution function associated with the αth discrete velocity $\boldsymbol{\xi}_\alpha$ and $f_\alpha^{(\text{eq})}$ is the corresponding equilibrium distribution function in the discrete velocity space. The nine-velocity square lattice model, which is often referred to as the 2-D 9-velocity (D2Q9) model [28] (Fig. 1), has been widely and successfully used for simulating two-dimensional (2-D) flows. In the D2Q9 model, $\boldsymbol{e}_\alpha$ denotes the discrete velocity set, namely,

$$\begin{aligned}
&\boldsymbol{e}_0 = 0,\\
&\boldsymbol{e}_\alpha = c(\cos((\alpha-1)\pi/4), \quad \sin((\alpha-1)\pi/4))\\
&\qquad \text{for } \alpha = 1,3,5,7,\\
&\boldsymbol{e}_\alpha = \sqrt{2}c(\cos((\alpha-1)\pi/4), \quad \sin((\alpha-1)\pi/4))\\
&\qquad \text{for } \alpha = 2,4,6,8,
\end{aligned} \tag{3}$$

where $c = \delta x/\delta t$, δx and δt are the lattice constant and the time step size, respectively. The equilibrium distribution for D2Q9 model is of the form

$$f_\alpha^{(\text{eq})} = \rho w_\alpha \left[1 + \frac{3}{c^2}\boldsymbol{e}_\alpha \cdot \boldsymbol{u} + \frac{9}{2c^4}(\boldsymbol{e}_\alpha \cdot \boldsymbol{u})^2 - \frac{3}{2c^2}\boldsymbol{u} \cdot \boldsymbol{u}\right], \tag{4}$$

where w_α is the weighting factor given by

$$w_\alpha = \begin{cases} 4/9, & \alpha = 0,\\ 1/9, & \alpha = 1,3,5,7,\\ 1/36, & \alpha = 2,4,6,8. \end{cases} \tag{5}$$

In the discretized velocity space, the density and momentum fluxes can be evaluated as

$$\rho = \sum_{\alpha=0}^{8} f_\alpha = \sum_{\alpha=0}^{8} f_\alpha^{(\text{eq})} \tag{6}$$

and

$$\rho\boldsymbol{u} = \sum_{\alpha=1}^{8} \boldsymbol{e}_\alpha f_\alpha = \sum_{\alpha=1}^{8} \boldsymbol{e}_\alpha f_\alpha^{(\text{eq})}. \tag{7}$$

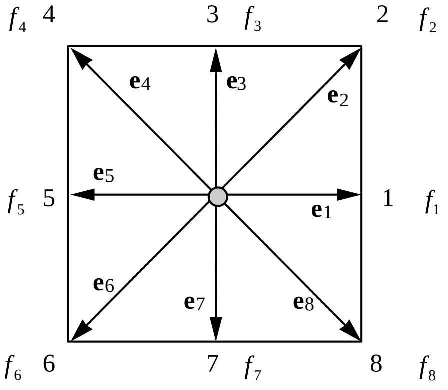

Fig. 1. A 2-D 9-velocity lattice (D2Q9) model.

The speed of sound in this model is $c_s = c/\sqrt{3}$ [28] and the equation of state is that of an ideal gas,

$$p = \rho c_s^2. \tag{8}$$

Qian et al. [28] also developed various models for 3-D flows with $f_\alpha^{(eq)}$ given in the same form as in Eq. (4). Depending on the number of the lattice velocity vectors used in these models, they are referred as D3Q15, D3Q19, and D3Q27 models.

Eq. (2) is called the discrete velocity model (DVM). The DVM was first introduced by Broadwell [34,35]. Further progress in the developments of DVM can be found, for example, in [36–43]. Numerically, it can be solved using any standard, practical method such as finite difference [44–47]. In using finite difference formulation, one needs to be careful about reducing the numerical diffusion associated with the discretization of the advection term and the stiffness of the differential equation when $\lambda \ll 1$ is required for low viscosity flows.

In the LBE method, Eq. (2) is discretized in a very special manner. The completely discretized equation, with the time step δt and space step $\delta x = \boldsymbol{e}_\alpha \delta t$, is

$$f_\alpha(\boldsymbol{x}_i + \boldsymbol{e}_\alpha \delta t, t + \delta t) - f_\alpha(\boldsymbol{x}_i, t) = -\frac{1}{\tau}\left[f_\alpha(\boldsymbol{x}_i, t) - f_\alpha^{(eq)}(\boldsymbol{x}_i, t)\right], \tag{9}$$

where $\tau = \lambda/\delta t$, and $\boldsymbol{x}_i$ is a point in the discretized physical space. Eq. (9), termed the LBE [25] with BGK approximation or LBGK model, is usually solved in the following two steps:

$$\text{collision step}: \tilde{f}_\alpha(\boldsymbol{x}_i, t + \delta t) = f_\alpha(\boldsymbol{x}_i, t) - \frac{1}{\tau}[f_\alpha(\boldsymbol{x}_i, t) - f_\alpha^{(eq)}(\boldsymbol{x}_i, t)], \tag{10a}$$

$$\text{streaming step}: \; f_\alpha(\boldsymbol{x}_i + \boldsymbol{e}_\alpha \delta t, t + \delta t) = \tilde{f}_\alpha(\boldsymbol{x}_i, t + \delta t), \tag{10b}$$

where $\tilde{f}_\alpha$ represents the post-collision state. It needs to be emphasized that with such a splitting in the computational procedure, there is no need to store both $f_\alpha(\boldsymbol{x}_i, t + \delta t)$ and $f_\alpha(\boldsymbol{x}_i, t)$ during the computation. Information on one time level is sufficient for unsteady flow simulations.

In order to derive the NS equations from LBE, the Chapman–Enskog expansion [48] is used. In essence, it is a standard multi-scale expansion [20], with time and space being rescaled as

$$t_1 = \varepsilon t, \quad t_2 = \varepsilon^2 t, \quad x_1 = \varepsilon x,$$
$$\frac{\partial}{\partial t} = \varepsilon \frac{\partial}{\partial t_1} + \varepsilon^2 \frac{\partial}{\partial t_2}, \quad \frac{\partial}{\partial x} = \varepsilon \frac{\partial}{\partial x_1} \tag{11}$$

and the particle distribution function f_α expanded as

$$f_\alpha = f_\alpha^{(0)} + \varepsilon f_\alpha^{(1)} + \varepsilon^2 f_\alpha^{(2)} + O(\varepsilon^3). \tag{12}$$

In the incompressible flow limit, $|\boldsymbol{u}|/c_s \ll 1$, the conservation principles of mass and momentum yield

$$\frac{\partial u_\alpha}{\partial x_\alpha} = 0, \tag{13}$$

$$\frac{\partial u_\alpha}{\partial t} + u_\beta \frac{\partial u_\alpha}{\partial x_\beta} = -\frac{1}{\rho}\frac{\partial p}{\partial x_\alpha} + v\nabla^2 u_\alpha. \tag{14}$$

The corresponding viscosity in the NS equation (14) derived from Eq. (9) is [28]

$$v = (\tau - 1/2)c_s^2 \delta t. \tag{15}$$

The modification of viscosity (from $v = \lambda c_s^2$ in Eq. (1)) corrects for the truncation error in the discretization of Eq. (2) and makes formally the LBGK scheme a second-order method for solving incompressible flows [32,33]. The positivity of the viscosity requires that $\tau > \frac{1}{2}$ in all LBE computations.

It is noted that the pressure p is obtained through an equation of state (Eq. (8)). The collision step is completely local. The streaming step involves no computation. Eq. (9) is explicit, easy to implement, and straightforward to parallelize.

As a computational tool, LBE method differs from NS equations based method in various aspects. The major differences are as follows:

1. NS equations are second-order partial differential equations (PDEs); the DVM from which the LBE model is derived consists of a set of first-order PDEs. Such a difference in the nature of PDE's is also reflected in the discretized forms for each type of equations.
2. NS solvers inevitably need to treat the nonlinear convective term, $\boldsymbol{u} \cdot \nabla \boldsymbol{u}$; the LBE method totally avoids the nonlinear convective term, because the convection becomes simple advection (uniform data shift).
3. CFD solvers for the incompressible NS equations need to solve the Poisson equation for the pressure. This involves global data communication, while in the LBE method data communication is always local and the pressure is obtained through an equation of state.
4. In the LBE method, the Courant-Friedrichs-Lewy (CFL) number is proportional to $\delta t/\delta x$, in other words, the grid CFL number is equal to 1 based on the lattice units of $\delta x = \delta t = 1$. Consequently, the time dependent LBE method is inefficient for solving steady-state problems, because its speed of convergence is dictated by acoustic propagation, which is very slow.
5. Boundary conditions involving complicated geometries require careful treatments in both NS and LBE solvers. In NS solvers, normal and shear stress

components require appropriate handling of geometric estimates of normal and tangent, as well as one-sided extrapolation. In LBE solvers, the boundary condition issue arises because the continuum framework, such as the no-slip condition at the wall, does not have a counterpart.

6. Since the Boltzmann equation is kinetic-based, the physics associated with the molecular level interaction can be incorporated more easily in the LBE model. Hence, the LBE model can be fruitfully applied to micro-scale fluid flow problems.
7. The spatial discretization in the LBE method is dictated by the discretization of the particle velocity space. This coupling between discretized velocity space and configuration space leads to regular square grids. This is a limitation of the LBE method, especially for aerodynamic applications where both the far field boundary condition and the near wall boundary layer need to be carefully implemented.

Because of the attractive features mentioned above, the LBE method has been particularly successful in simulations of fluid flows involving complicated boundaries or/and complex fluids, such as turbulent external flow over structures with complicated geometries [49], Rayleigh–Taylor instability between two fluids [50], multi-component fluids through porous media [51], particle suspensions in fluid [52–70], chemically reacting flows [71], combustions [72], magnetohydrodynamics [73], crystallization [74,75], and others [15,12].

There have been efforts to extend the LBE method for higher Reynolds number computations [76–81] with the hope that it can efficiently solve aerodynamics problems. However, to extend the LBE method for high Reynolds number flows, several issues, which include force evaluation for flow over a curved body, reconciliation of resolution requirement for different flow regions, accurate treatment for curved boundary, numerical stability, and finally turbulence models, must be addressed. The first four issues will be discussed first in this review. The most recent efforts to address these issues will be highlighted. The turbulence model in the LBE method will be discussed in the last section along with the recent development and applications of LBE method for thermal fluid flows, multi-phase and multi-component flows, particulate suspensions, and micro-flows.

1.2. Computational issues of the LBE method

1.2.1. Force evaluation

The evaluation of the force on a body in a flow field is a common task in fluid mechanics research efforts. This is also the case for computations using the LBE method. Different force evaluation schemes, including momentum exchange [52,53,91] and integration of stress [82,83], have been used to evaluate the fluid dynamic force on a curved body in the context of the LBE method. In Fig. 2, a curved wall separates the solid region from the fluid region. The lattice node on the fluid side of the boundary is denoted as $\boldsymbol{x}_{\mathrm{f}}$ and that on the solid side is denoted as $\boldsymbol{x}_{\mathrm{b}}$. The filled small circles on the boundary, $\boldsymbol{x}_{\mathrm{w}}$, denote the intersections of the wall with various lattice links. The boundary velocity at $\boldsymbol{x}_{\mathrm{w}}$ is $\boldsymbol{u}_{\mathrm{w}}$. The fraction of an intersected link in the fluid region is Δ, that is,

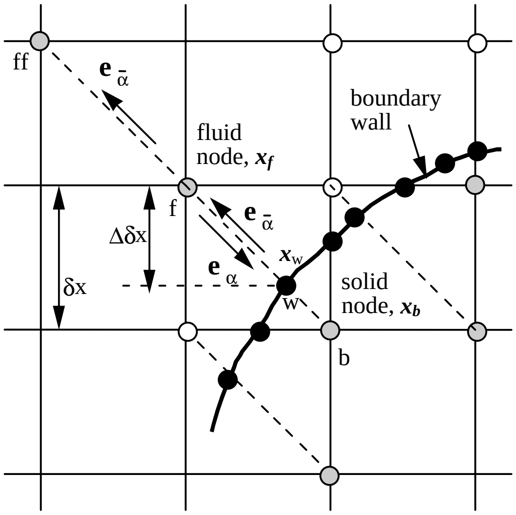

Fig. 2. Layout of the regularly spaced lattices and curved wall boundary.

$$\Delta = \frac{|\boldsymbol{x}_{\mathrm{f}} - \boldsymbol{x}_{\mathrm{w}}|}{|\boldsymbol{x}_{\mathrm{f}} - \boldsymbol{x}_{\mathrm{b}}|}, \quad 0 \leqslant \Delta \leqslant 1. \tag{16}$$

The horizontal or vertical distance between $\boldsymbol{x}_{\mathrm{b}}$ and $\boldsymbol{x}_{\mathrm{w}}$ is $\Delta\delta x$ on the square lattice. The particle momentum moving from $\boldsymbol{x}_{\mathrm{f}}$ to $\boldsymbol{x}_{\mathrm{b}}$ is $\boldsymbol{e}_{\alpha}$ and the reversed one from $\boldsymbol{x}_{\mathrm{b}}$ to $\boldsymbol{x}_{\mathrm{f}}$ is $\boldsymbol{e}_{\bar{\alpha}} = -\boldsymbol{e}_{\alpha}$. The method of integration of stress requires great details of the surface geometry, and an extensive use of extrapolation of stress from neighboring $\boldsymbol{x}_{\mathrm{f}}$ to $\boldsymbol{x}_{\mathrm{w}}$. It can be laborious to program for 3-D problems. The momentum exchange method basically involves adding $\tilde{f}_{\bar{\alpha}}(\boldsymbol{x}_{\mathrm{b}})$ with $\tilde{f}_{\alpha}(\boldsymbol{x}_{\mathrm{b}} + \boldsymbol{e}_{\bar{\alpha}}\delta t)$ for all possible α and solid nodes. While the calculation is extremely simple the accuracy of the momentum exchange method for curved body needs to be examined at higher Reynolds numbers.

1.2.2. Reconciliation of resolution requirement

High resolution is often needed in the high gradient region, such as the near wall region in a high Reynolds number flow. This requires a small grid size near the wall. For external flows, the far field boundary often needs to be placed far away from the solid wall while the resolution can be lower. This immediately creates a difficulty for the original LBE method, which was based on constant grid size. In the NS equation-based solvers, this issue is easily resolved by using grid stretching techniques, often in a curvilinear coordinate system. To increase the numerical efficiency while maintaining accuracy in LBE, non-uniform grid has been introduced. He et al. [82] developed an interpolation scheme, which increases grid resolution in the high shear rate region. Mei and Shyy [45] used a finite difference formulation to solve the DVM given by Eq. (2) and D2Q9 model in a curvilinear coordinate system.

To maintain the inherent advantage of LBE method such as coding simplicity and computational efficiency, one prefers to employ the uniform lattice. Thus, to reconcile different requirements of grid resolution, it is desirable to divide computational domain into different regions. In each region, a constant lattice space can be used. In practical applications, there are two different treatments. The overlapped grid approach is that the whole computational domain is covered with coarse grids. The patches with fine grids are placed in the desired regions. In that context, Filippova and Hänel [83] developed a local grid refinement for the LBE method. In the abated grid approach there is only one grid in each region. This technique has been applied to the LBE method by Yu et al. [84].

1.2.3. Boundary conditions

Two classes of boundaries are frequently encountered in CFD: open boundaries and the solid wall. The open boundaries include lines (or planes) of symmetry, periodic cross-sections, infinity, and inlet and outlet. At these boundaries, velocity or pressure is usually specified in the macroscopic description of fluid flows.

A difficulty of the LBE method is that the boundary conditions for the distribution functions f_α's are not known. One must construct suitable conditions for f_α's based on the macroscopic flow variables. At the symmetric and periodic boundaries, the conditions for f_α's can be given without ambiguity. At the outlet of a computational domain, the condition can usually be given by simple extrapolation.

In general, the boundary condition for the velocity at a solid wall can only be satisfied approximately through solving f_α's. Right after the collision step, $\tilde{f}_\alpha(\boldsymbol{x}_\mathrm{f})$ at the node x_f on the fluid side (see Fig. 2) is known for all α, but $\tilde{f}_{\bar{\alpha}}(\boldsymbol{x}_\mathrm{b})$, the post-collision distribution function coming from a solid node $\boldsymbol{x}_\mathrm{b}$ to a fluid node $\boldsymbol{x}_\mathrm{f}$, is not known. To complete the subsequent streaming step, $\tilde{f}_{\bar{\alpha}}(\boldsymbol{x}_\mathrm{b}, t)$ is needed since it exactly gives $f_{\bar{\alpha}}(\boldsymbol{x}_\mathrm{f}, t+\delta t)$ after streaming. A popular approach is to employ the bounce-back scheme [85,86]. In this scheme, the momentum from the incoming particle, $\tilde{f}_\alpha(\boldsymbol{x}_\mathrm{f}, t)\boldsymbol{e}_\alpha$, is bounced back in the opposite direction after the particle hits the wall. For a stationary wall, it is equivalent to setting $\tilde{f}_{\bar{\alpha}}(\boldsymbol{x}_\mathrm{b}, t) = \tilde{f}_\alpha(\boldsymbol{x}_\mathrm{f}, t)$. For a moving wall, a certain amount of momentum should be added to the bounced particle. This results in

$$\tilde{f}_{\bar{\alpha}}(\boldsymbol{x}_\mathrm{b}, t) = \tilde{f}_\alpha(\boldsymbol{x}_\mathrm{f}, t) + 2w_\alpha\rho_\mathrm{w}\frac{3}{c^2}\boldsymbol{e}_{\bar{\alpha}}\cdot\boldsymbol{u}_\mathrm{w}$$

for the bounce-back scheme with a moving wall where ρ_w is the fluid density at the wall. Ladd [52,53] had shown that second-order accuracy for the non-slip condition can be achieved if the wall is placed in the middle of the lattice nodes, i.e. $\Delta = \frac{1}{2}$. Usually, it requires that the curved solid wall be approximated as a series of stair steps in this treatment.

Filippova and Hänel [83] developed a curved boundary treatment using Taylor series expansion in both space and time for f_α near the wall. This boundary condition satisfies the no-slip condition to the second order in δx and preserves the geometrical integrity of the wall boundary. In addition, two other boundary treatments for curved wall, one by Mei et al. [87] and the other by Bouzidi et al. [88] have also been proposed. All of those methods need to treat the boundary condition separately for $\Delta \leqslant \frac{1}{2}$ and $\Delta > \frac{1}{2}$. This will potentially cause abrupt change in f when Δ changes from smaller than $\frac{1}{2}$ to larger than $\frac{1}{2}$ in dealing with curved boundaries. A unified scheme for curved wall was recently developed by Yu et al. [89].

The bounce-back scheme for the solid wall has been directly extended to treat the inlet boundary when the inlet velocity is given [85,90–92]. While such a treatment is a straightforward extension of the solid wall condition, it also creates a mechanism for the pressure waves from the interior of the computational domain to interact with the inlet boundary and reflect back. Because the pressure wave propagation is typically of an inviscid nature, depending on the nonlinearity and complexity of the specific problem, this may provoke computational instability or prevent the spatial wiggles from being dissipated quickly during the course of computation. It is desirable to employ a suitable boundary condition for f_α's which can reduce the interaction at the inlet boundary. Such an inlet condition has been recently proposed by Yu [116].

1.2.4. Numerical stability and dispersion

Computational stability and dispersion are major issues in many fluid dynamics computations. The simplest LBE is based on the BGK model, which involves the SRT approximation. In contrast to the SRT approximation, the multi-relaxation-time (MRT) (also called generalized) LBE method has been proposed by d'Humières [30] and examined more recently by Lallemand and Luo [93]. The basic idea is that in the SRT model, the bulk and shear viscosities are both determined by the same relaxation time. The MRT model attempts to relax different modes with different relaxation times so that the bulk and shear viscosities can be determined by different relaxation times and adjusted independently. In LBE computations spurious pressure waves are often generated because of poor initial condition or geometric singularity. Large bulk viscosity can help dampen such spurious waves [94] while maintaining the low shear viscosity, and thus improve the accuracy of the unsteady solution or the convergence toward steady state. However, there is little difference in the performances on the high wave-number range as suggested by the theoretical analysis in Lallemand and Luo [93]. Computationally, a key question is whether the MRT model can improve the numerical stability via reducing the dispersion errors (or wiggles) without increasing the computational cost. Mei et al. examined the performance of the 2-D SRT and MRT models in detail for flows with singularity [95].

The present review offers an updated account of the technique developed to address the above-mentioned issues. Both theoretical development and computational assessment will be highlighted to offer a comprehensive view of the state-of-the-art. This paper is structured as follows. In Section 2, methods for evaluating force (drag and lift) on a body are discussed. Section 3 presents the concepts related to the multi-block techniques, with special attention paid to ensure the conservation of mass and momentum fluxes across the interface between blocks. In Section 4, suitable boundary treatment strategies are discussed for irregularly shaped solid walls. In Section 5, recent progress on open boundary condition is discussed. In Section 6, a multi-relaxation-time LBE model is introduced along with the demonstration that this model can substantially reduce the spatial oscillations observed in the high Reynolds number flow solutions. In Section 7, perspectives on applying LBE for thermal fluid flows, multi-phase and multi-component flows, particulate suspensions, turbulent flows, and micro-flows are offered. Finally, concluding remarks are provided in Section 8.

2. Force evaluation on a solid body

Fluid–boundary interaction is a key issue in the LBE method. Fluid force on the curved boundary is a basic quantity of interest. Proper evaluation of the fluid force is also essential in assessing various developments in the LBE method. Since the issue of force evaluation will show up frequently in the rest of this article, it is discussed first.

2.1. Stress integration approach

While the momentum exchange method is unique to the LBE method, the stress integration on a curved surface has been widely used in the NS equation-based solvers. He and Doolen [79] evaluated the force by integrating the total stresses on the surface of the cylinder:

$$F = \int \tilde{\boldsymbol{n}} \cdot [p\underline{\boldsymbol{I}} + \rho\nu(\nabla\boldsymbol{u} + (\nabla\boldsymbol{u})^{\mathrm{T}})]\,\mathrm{d}A. \tag{17}$$

In their study, a body-fitted coordinate system together with grid stretching was used such that a large number of nodes can be placed near the body to accurately compute the velocity gradient $\nabla\boldsymbol{u}$. In general, since $\boldsymbol{u}$ is not the primary variable in the LBE simulations and the evaluation of $\boldsymbol{u}$ using Eq. (7) based on f_α's suffers the loss of accuracy due to the round-off errors, the evaluation of the gradient can result in further degradation of the accuracy. Filippova and Hänel [83] used a similar integration scheme to obtain the dynamic force on the body for the force on a circular cylinder except that the deviatoric stresses were evaluated using the non-equilibrium part of the particle distribution function (see Eq. (19) below). However, since the Cartesian grid was used, the stress vectors on the surface of the body (with arbitrary Δ) had to be computed through an extrapolation procedure. This can lead to further loss of accuracy for finite lattice size δx when the shear layer near the wall is not sufficiently resolved.

In Eq. (17), the pressure p can be easily evaluated using Eq. (8). For D2Q9 and D3Q19 models $c_s^2 = \frac{1}{3}$ so that $p = \rho/3$. The deviatoric stress for incompressible flow

$$\tau_{ij} = \rho\nu(\nabla_i\boldsymbol{u}_j + \nabla_j\boldsymbol{u}_i) \tag{18}$$

can be evaluated using the non-equilibrium part of the distribution function as

$$\tau_{ij} = \left(1 - \frac{1}{2\tau}\right)\sum_{\alpha=1}^{8}[f_\alpha(\boldsymbol{x},t) - f_\alpha^{(\mathrm{eq})}(\boldsymbol{x},t)] \times \left(\boldsymbol{e}_{\alpha i}\boldsymbol{e}_{\alpha j} - \frac{1}{2}\boldsymbol{e}_\alpha\cdot\boldsymbol{e}_\alpha\delta_{ij}\right). \tag{19}$$

In the above, $f_\alpha - f_\alpha^{(\mathrm{eq})}$ is the non-equilibrium part, $f_\alpha^{(\mathrm{neq})}$, of particle distribution function f_α. If the surface stress integration method is to be used, Eq. (19) is clearly superior to Eq. (18).

In a study by Mei et al. [96], the variation of the pressure on the surface of a circular cylinder at finite Reynolds number was examined in order to gain an insight into the method of surface stress integration. The computation was carried out using the LBE method for flow over a column of cylinders. Fig. 3 shows the pressure coefficient, $C_p = 2(p - p_\infty)/(\rho U^2)$, where p_∞ is the far upstream pressure, on the surface obtained by using a second-order extrapolation in the LBE simulation. The 3-D multi-block, body-fitted coordinates, and pressure-based Navier–Stokes solver [97–99] with a much finer resolution: 201 points around the cylinder and the smallest grid size along the radial direction $\delta r = 0.026$ (relative to the radius $r = 1$) were used. It gave

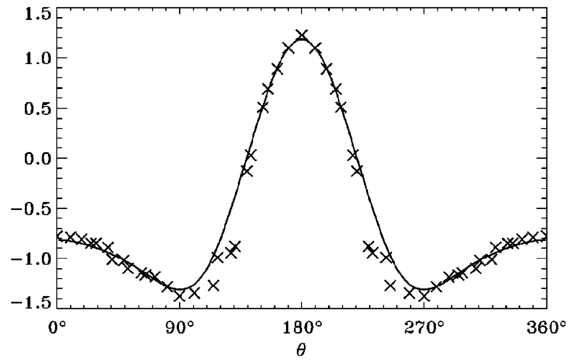

Fig. 3. Distribution of the pressure coefficient CP on the surface of a 2-D circular cylinder of radius $r = 6.6$, and center-to-center distance $H/r = 20$. The stagnation point is located at $\theta = 180°$. The LBE result denoted by symbol × is obtained with $\tau = 0.6$ and $Re = 40$. The solid line is the result obtained by using a 3-D multi-block, body-fitted grid, and pressure-based NS solver with a much finer resolution [96].

smoother pressure variation than the LBE result with a Cartesian grid of coarser resolution. Nevertheless, the LBE solution still essentially agrees with the NS solution. The components of the deviatoric stress tensor show a similar, noisy pattern. It is not clear how the noise in the pressure and stresses affect the accuracy of the fluid dynamic force in the stress integration method. While the programming in the extrapolation and integration is manageable in 2-D cases, it is rather tedious in 3-D cases.

2.2. Momentum exchange approach

Instead of the stress integration method, Ladd [53] used the momentum exchange method to compute the fluid force on a sphere in suspension flow. In the flow simulation using the bounce-back boundary condition, the body is effectively replaced by a series of stairs. Each segment on the surface has an area of unity for a cubic lattice. The force on each link (halfway between fluid lattices at $\mathbf{x}_f$ and solid lattice at $\mathbf{x}_b = (\mathbf{x}_f + \mathbf{e}_\alpha \delta t)$; see Fig. 2 for the definitions of $\mathbf{x}_f$ and $\mathbf{x}_b$) results from the momentum exchange (per unit time) between two opposing directions of the neighboring lattices, $[\mathbf{e}_{\bar\alpha}\tilde{f}_{\bar\alpha}(\mathbf{x}_b, t) - \mathbf{e}_\alpha \tilde{f}_\alpha(\mathbf{x}_f = \mathbf{x}_b + \mathbf{e}_{\bar\alpha}\delta t, t)]\delta x/\delta t$. The total force acting on a solid body by fluid is obtained as

$$\mathbf{F} = \sum_{\text{all } \mathbf{x}_b} \sum_{\alpha=1}^{N_d} \mathbf{e}_{\bar\alpha}[\tilde{f}_\alpha(\mathbf{x}_b, t) + \tilde{f}_{\bar\alpha}(\mathbf{x}_b + \mathbf{e}_{\bar\alpha}\delta t, t)] \times [1 - w(\mathbf{x}_b + \mathbf{e}_{\bar\alpha})]\delta x/\delta t, \tag{20}$$

where N_d is the number of non-zero lattice velocity vectors and $w(\mathbf{x}_b + \mathbf{e}_{\bar\alpha})$ is an indicator, which is 0 at $\mathbf{x}_f$ and 1 at $\mathbf{x}_b$. This indicator is used in Eq. (20) for illustration purpose and the actual computation does not need to involve $w(\mathbf{x}_b + \mathbf{e}_{\bar\alpha})$. The inner summation calculates the momentum exchange between a solid node at $\mathbf{x}_b$ and all possible neighboring fluid nodes around that solid node. The outer summation calculates the force contributed by all boundary nodes $\mathbf{x}_b$. Eq. (20) is applicable for both 2-D and 3-D LBE models. Whereas the momentum exchange method is easy to implement computationally, its accuracy for a curved boundary has not been systematically studied previously.

2.3. Comparison of two force evaluation approaches

The momentum exchange method was proposed for the case with $\Delta = \frac{1}{2}$ at every boundary intersection $\mathbf{x}_w$. Whether this scheme can be applied to the case with $\Delta \neq \frac{1}{2}$ when, for example, the geometry is not straight, needs to be investigated. Furthermore, as in the case of stress integration method, the resolution near a solid body is often insufficient and the profiles of the near wall flow variables can be noisy.

Mei et al. [96] compared the performance of two force valuation schemes. In their study, flows over a column of cylinders (2-D) and over a sphere (3-D) were simulated. On the surface of solid body, a second-order curved boundary treatment was used [87]. For a uniform flow over a column of circular cylinders of radius r with center-to-center distance denoted by H (see the left part of Fig. 5), symmetry conditions for f_α's are imposed at $y = \pm H/2$. Details of flow field simulations can be found in Mei et al. [87]. The Reynolds number is defined by the diameter of the cylinder d as $Re = Ud/\nu$, where U is the uniform velocity at the inlet. The drag coefficient over a circular cylinder of radius r is defined as

$$C_D = \frac{|F_x|}{\rho U^2 r}. \tag{21}$$

Fig. 4a compares C_D obtained from momentum exchange method, surface stress integration, and finite difference result of Fornberg [100] using a vorticity-stream function formulation at $Re = 100$, $H/r = 20$, for r ranging from 2.8 to 13.2. For $r > 8$, both momentum exchange and the stress integration give satisfactory results for C_D in comparison with the value of 1.248 given by Fornberg [100]. The small difference in C_D could be due to the fact that in Fornberg's study, the computational domain in downstream direction is about 10 times larger than that adopted by Mei et al. [96]. This adds credence to the validity of using momentum exchange evaluating the total force on a curved body. The values of C_D from the momentum exchange method have less scattering than those from the stress integration. Accepting an error of less than 5%, reliable data for C_D can be obtained, using the momentum exchange method, for $r > 5$. That is, 10 lattices cross the diameter of the cylinder are necessary to obtain reliable values of the force. This is consistent with the finding of Ladd [53]. In the range of $5 < r < 7$, the stress integration method gives more scattered result than the method of momentum exchange. For smaller radius, i.e., insufficient lattice resolution, while both methods give poor results, the stress integration yields much larger errors.

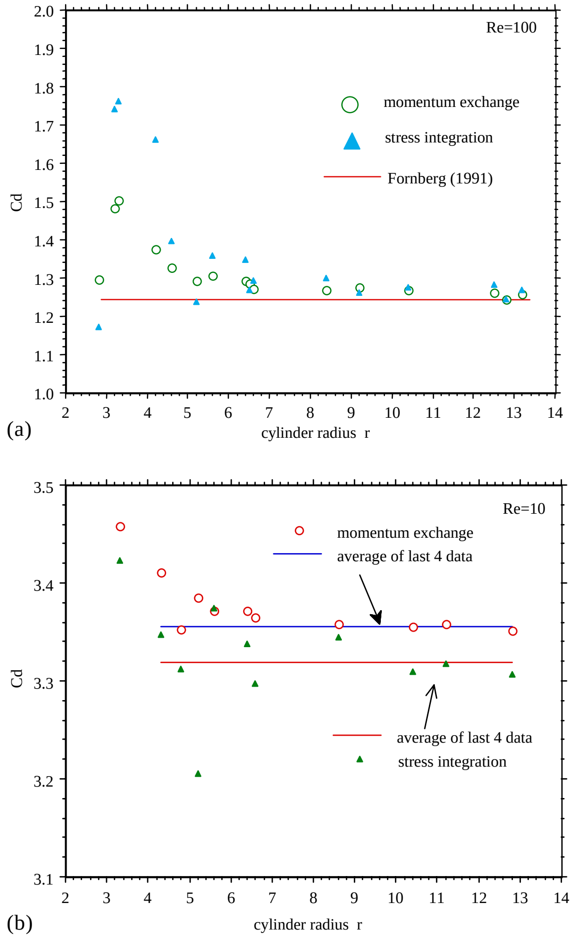

Fig. 4. Drag coefficient for a uniform flow over a column of cylinders over a range of radius r (a) $Re = 100$ and (b) $Re = 10$ [96]. For $Re = 100$, Benchmark solution was given by Fornberg [100].

Fig. 4b compares C_D obtained from the methods of momentum exchange and stress integration for $Re = 10$. The momentum exchange method seems to give a converged result for $r > 8$ with an average value of $C_D \sim 3.356$. In contrast, the stress integration method has a larger scattering than momentum exchange method. Averaging over the result for $r > 8$, the stress integration gives $C_D \sim 3.319$. The difference between converged results of two methods is about 1%. For r less than or around 5, the scattering in C_D from the stress integration method is much larger than that in the momentum exchange method. The conclusions from the comparisons in Fig. 4 are as follows: (i) both methods for force evaluation can give accurate results; (ii) the momentum exchange method gives more consistent drag estimates; (iii) in the range of $10 < Re < 100$, a resolution of 10 lattices across the diameter of the cylinder is needed in order to obtain reliable drag values.

In the steady uniform flow over a sphere simulation, to limit the computational effort, a finite domain: $-H/2 \leqslant y \leqslant H/2$ and $-H/2 \leqslant z \leqslant H/2$ with $H/r = 10$ was used to compute the flow over a sphere of radius r (Fig. 5) [101]. Two cases were considered. One was to simulate an unbounded flow over the sphere. The other was to simulate flow over a planer array of sphere (all located at $x = 0$) with the center of the spheres forming square lattices.

For flow over a sphere, the drag coefficient is often expressed as

$$C_D = \frac{-F_x}{\frac{1}{2}\rho U^2 \pi r^2} = \frac{24}{Re}\phi \quad \text{or} \quad \phi = \frac{-F_x}{6\pi\mu U r}, \tag{22}$$

where ϕ accounts for the non-Stokesian effect of the drag. For two types of the boundary conditions at $(y = \pm H/2, z = \pm H/2)$, $\phi_{\rm sym}$ is used to denote the non-Stokesian correction for the case where the symmetry conditions are imposed at $(y = \pm H/2, z = \pm H/2)$ and $\phi_{\rm unb}$ is used to denote the results for the case where the extrapolation for f_α's is used at $(y = \pm H/2, z = \pm H/2)$ in order to simulate the unbounded flow. The D3Q19 model was used.

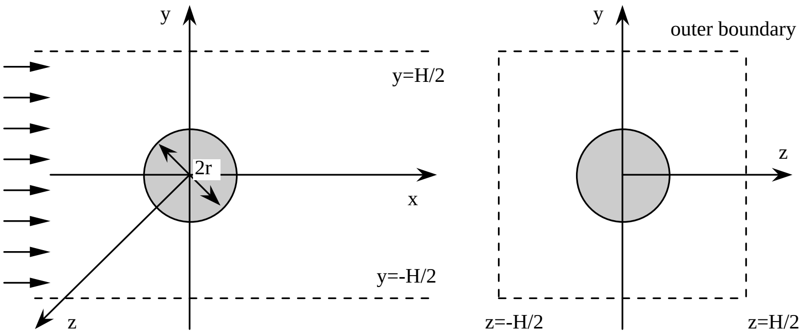

Fig. 5. Schematic for uniform flow over a sphere.

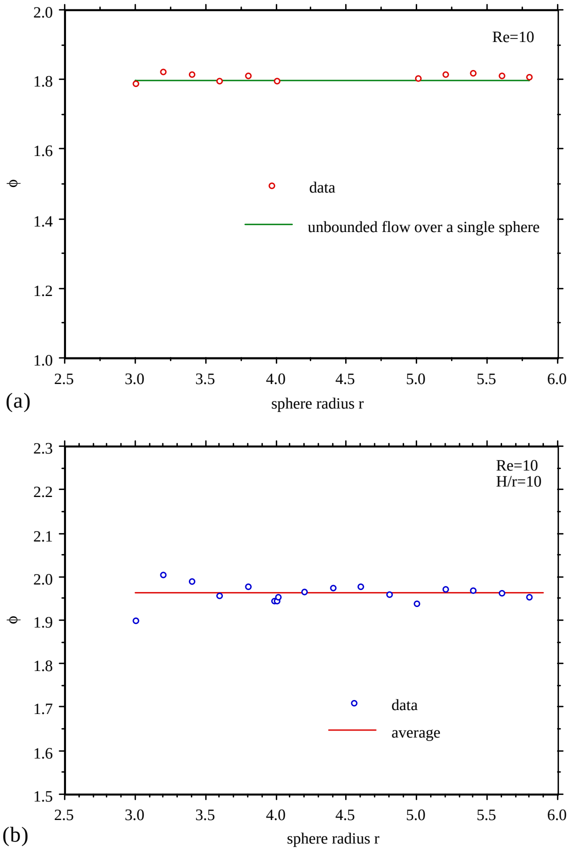

Fig. 6. Variation of the non-Stokesian correction factor with sphere radius at $Re = 10$ [96]. (a) Flow over a single sphere in an unbounded field [96]. (b) Flow over a planer array of spheres. Data are from the LBE simulations.

Fig. 6a shows the non-Stokesian coefficient ϕ_{unb} for $r = 3.0, 3.2, 3.4, 3.6, 3.8, 4.0, 5.1, 5.2, 5.4, 5.6$ and 5.8 for $H/r = 10$ at $Re = 10$. The relaxation time is $\tau = 0.7$. In this range, the number of the boundary nodes on the surface of the sphere increases roughly by a factor of $(5.8/3)^2 \sim 3.74$; the actual counts of the boundary nodes $\boldsymbol{x}_b$ gives a ratio $2370/546 = 4.35$. The largest difference is 1.9% between $r = 3.0$ and 3.2 which have the least resolution in the series investigated. For a uniform flow over an unbounded sphere, an independent computation using a finite difference method based on the vorticity-stream function formulation with high resolution gave a non-Stokesian coefficient $\phi \sim 1.7986$ at $Re = 10$. The largest difference between this result and the LBE results is 1.36% at $r = 3.2$. If the LBE data for the drag is averaged over the range of r, one obtains $\phi \sim 1.8086$ which differs from 1.7986 by 0.54%. Hence, the LBE solutions based on $r = 3.0 - 5.8$ give quite consistent drag force.

Fig. 6b shows the non-Stokesian correction factor ϕ_{sym} for a uniform flow over a planar array of spheres for $r = 3.0-5.8$ for $H/r = 10$ and $Re = 10$. It is important to note that with the improvement of the surface resolution by a factor of 4.35, there is little systematic variation in $\phi_{\text{sym}}(r)$. The largest deviation from the average value, $\phi_{\text{sym,ave}} \sim 1.963$, is 1.1% at $r = 5.0$. It is clear that the LBE solution gives reliable fluid dynamic force on a sphere at $r \sim 3.5$ for a moderate value of Re. The set of data for ϕ_{sym} is inherently more consistent than that for ϕ_{unb} since the symmetry boundary condition can be exactly specified at $(y = \pm H/2, z = \pm H/2)$ while the extrapolation conditions do not guarantee the free stream condition at $(y = \pm H/2, z = \pm H/2)$. Yet, both ϕ_{unb} and ϕ_{sym} exhibit remarkable self-consistency from coarse to not-so-coarse resolutions.

In summary, the momentum exchange method is very simple to implement. In 2-D and 3-D flows over a bluff body, it can give reliable values when there are at least 10 lattices across the body at $Re \sim 100$. The method of integrating the stresses on the surface of the body gives similar result when there is sufficient resolution but a much larger uncertainty exists when the resolution is limited in comparison with the method of momentum exchange. In addition, this method requires considerably more efforts in implementing the extrapolation and integration on the body surface in comparison with the method of momentum exchange. The method of momentum exchange is thus recommended for force evaluation on curved bodies.

3. Local grid refinement and multi-block methods

To enhance the numerical efficiency and accuracy, the non-uniform grid has been introduced into the LBE method. He et al. [82] solved the discretized, two-step LBE Eq. (10) on non-uniform grid. In their method, both the evaluation of the physical variables and the relaxation step were carried out at the grid points. The streaming step, Eq. (10b), carries f_α's to non-grid points. A spatial interpolation was supplemented to obtain the post-streaming f_α's to the grid points. As shown in Lallemand and Luo [93], this interpolation may introduce extra numerical diffusion. Mei and Shyy [45] employed curvilinear coordinate system to solve the DVM Eq. (2) using a finite difference formulation. In the work of Tolke et al. [46], the DVM was also solved in finite difference form and a grid refinement procedure was developed. Kandhai et al. [47] proposed a multiply nested lattice strategy to solve the DVM in finite difference form. Bouzidi et al. [102] presented a 2-D rectangular lattice model in an attempt to achieve an arbitrary grid aspect ration in the LBE method.

3.1. Local grid refinement scheme and interface information exchange

Filippova and Hänel [83] proposed a local refinement method for solving Eq. (9) so that the advantage of LBE method can mostly be retained. In their method, patches of fine grids were used in certain regions, for examples, around a solid body. The simulation was first carried out on the coarse grid level with a smaller relaxation time, allowing a rapid propagation of boundary information throughout the entire domain. At a later time, the computation on the fine grid variables was initiated. The dependent variables on both grid levels were, then, advanced in time simultaneously with the fine grid boundary conditions obtained from the base grid solution at the grid interface.

In transferring information among various blocks of different lattice size, proper rescaling of f_α's is essential in order to satisfy the conservation of mass and momentum and continuity of stresses across the interface joining two grid systems. The interface information exchange schemes derived by Filippova and Hänel [83] are described below.

For a given lattice size δx, the viscosity of the fluid is

$$v = (2\tau - 1)\delta_x c/6. \tag{23}$$

In order to keep a consistent viscosity, and thus Re, in the entire flow field involving different lattice sizes, the relation between relaxation times, τ_f, on the fine grid of grid size δx_f, and τ_c, on the coarse grid of grid size δx_c, must obey the following rule:

$$\tau_\mathrm{f} = \frac{1}{2} + m\left(\tau_\mathrm{c} - \frac{1}{2}\right), \tag{24}$$

where $m = \delta x_\mathrm{c}/\delta x_\mathrm{f}$ is the grid size ratio. To keep the variables and their derivatives continuous across an interface between two different grids, a consistent and accurate relationship for f_α's in the neighboring blocks were developed as

$$\tilde{f}_\alpha^{(\mathrm{c})} = f_\alpha^{(\mathrm{eq,f})} + m\frac{\tau_\mathrm{c} - 1}{\tau_\mathrm{f} - 1}\left[\tilde{f}_\alpha^{(\mathrm{f})} - f_\alpha^{(\mathrm{eq,f})}\right], \tag{25}$$

$$\tilde{f}_\alpha^{(\mathrm{c})} = f_\alpha^{(\mathrm{eq,c})} + \frac{\tau_\mathrm{f} - 1}{m(\tau_\mathrm{c} - 1)}\left[\tilde{f}_\alpha^{(\mathrm{c})} - f_\alpha^{(\mathrm{eq,c})}\right]. \tag{26}$$

A flow over an asymmetrically placed cylinder in the channel [103] was calculated with the grid refinement around the cylinder by Filippova and Hänel [83]. Fig. 7 shows an instantaneous pressure contour. Fig. 8 compares the drag and lift coefficients, $C_\mathrm{D} = F_x/\rho\bar{U}^2 r$ and $C_\mathrm{L} = F_y/\rho\bar{U}^2 r$, in which F_x and F_y are the x- and y-components of the force on the cylinder, $\bar{U}$ is the average inlet velocity, and r is the radius of cylinder, obtained using both the bounce-back and their curved boundary condition with results given by Schäfer and Turek [103]. Lin and Lai [104] applied the method of Filippova and Hänel to the 2-D lid-driven cavity flow and showed that this method can improve the efficiency in computation.

3.2. Multi-block method

Yu et al. [84] applied the multi-block technique to the LBE method. In this method, flow field is divided into blocks. In each block, the grid spacing is uniform with desired resolution. In this multi-block method, the different grid size blocks are not overlapped between each other, and blocks are connected only thorough interface so that this method is different from the grid refinement method. The interface information exchange scheme given by Eqs. (25) and (26) is used. Furthermore, a systematic effort has been made to evaluate the performance of the multi-block method, including both accuracy and efficiency aspects with emphasis on the conservative properties across the interface and block-to-block coupling. In what follows, key elements in the interface treatment will be highlighted and results regarding the conservation laws on the interface are reviewed.

The typical interface structure is shown in Fig. 9. The line $\overline{\mathrm{MN}}$ is the fine grid block boundary, while the line $\overline{\mathrm{AB}}$ is the coarse grid block boundary. The coarse block boundary is in the interior of the fine block, and the fine block boundary is in the interior of the coarse block. This arrangement of the interface is convenient for the information exchange between two neighboring blocks. For example, grid Q is an interior lattice node of the coarse block. After the collision step, the values of incoming distribution functions $\tilde{f}_2(t^{n+1}, X_\mathrm{D})$,$\tilde{f}_3(t^{n+1}, X_\mathrm{E})$ and $\tilde{f}_4(t^{n+1}, X_\mathrm{F})$ from boundary nodes D, E, and F, respectively, are needed in order to obtain $f_2(t^{n+1}, X_\mathrm{Q})$,$f_3(t^{n+1}, X_\mathrm{Q})$ and $f_4(t^{n+1}, X_\mathrm{Q})$ at the end of

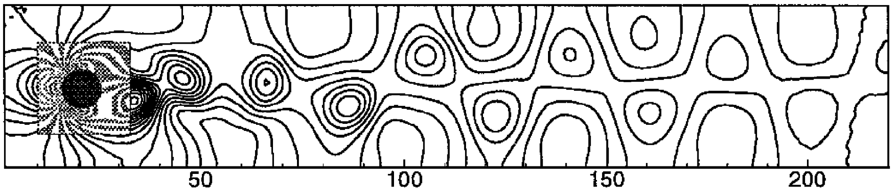

Fig. 7. Unsteady flow around a cylinder at $Re = 100$: instantaneous isobars computed by Filippova and Hänel [83] using local grid refinement technique.

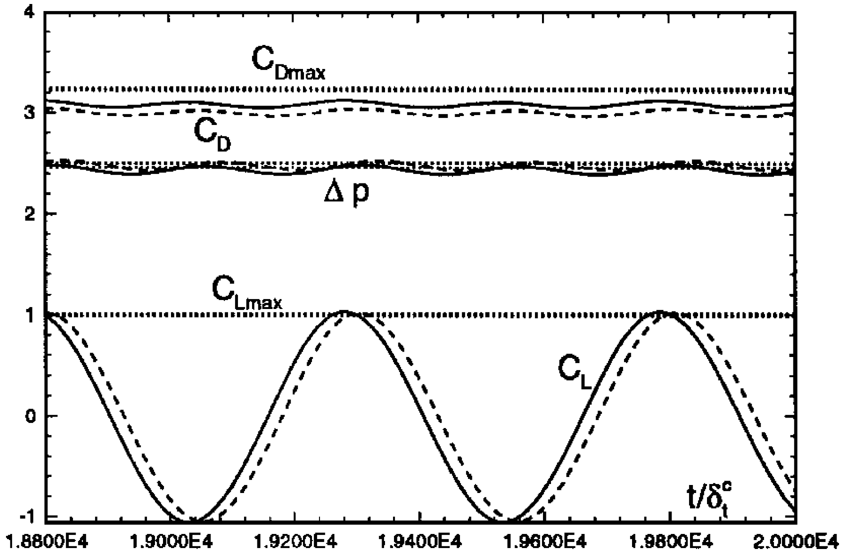

Fig. 8. Unsteady flow around a cylinder at $Re = 100$ computed by Filippova and Hänel [83]. Coefficients of drag C_D and lift C_L and pressure difference Δp between the front and end points of cylinder vs. the number of time steps in coarse grid: solid lines—boundary-fitting conditions; dashed lines—bouncing-back conditions; straight dotted lines—bounds of reference values $C_{D\,\max}$; $C_{L\,\max}$; $\Delta p/(t_0 + T/2)$ [103]. Reprinted from Journal of Computational Physics, Vol. 147, Filippova and Hänel, Grid refinement for lattice-BGK models, 219–228 (1998), with permission from Elsevier Science.

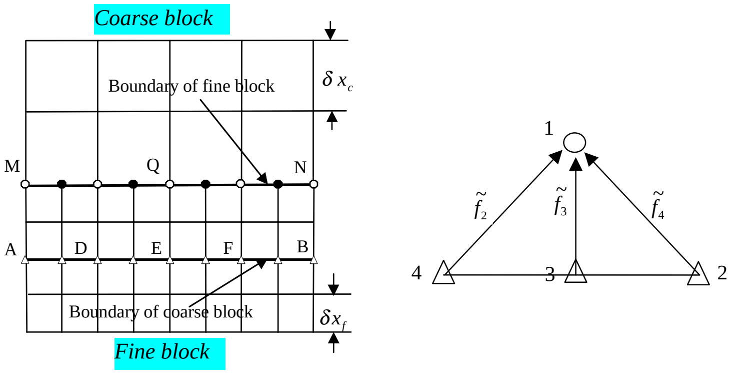

Fig. 9. Interface structure between two blocks of different lattice spacing [84].

steaming step since other components of $f_\alpha(t^{n+1}, X_Q), (\alpha = 1, 5, 6, 7, 8)$ are obtained from advecting the neighboring post-collision values of $\tilde{f}_\alpha$ in the interior nodes of the coarse block. For the same reason, the fine block boundary $\overline{MN}$ is located in the interior of the coarse block. However, on the fine block boundary $\overline{MN}$, there is no information on the nodes denoted by the solid symbol ● in Fig. 9; it needs be obtained through spatial interpolation based on the information at the nodes denoted by the open symbol ○ on $\overline{MN}$. To eliminate the possibility of asymmetry caused by interpolations, a symmetric, cubic spline fitting is used for spatial interpolation of $\tilde{f}_\alpha$ on the fine block boundary,

$$\tilde{f}(x) = a_i + b_i x + c_i x^2 + d_i x^3, \quad x_{i-1} \leqslant x \leqslant x_i, \; i = 1, \ldots, n \tag{27}$$

where the constants (a_i, b_i, c_i, d_i) are determined by using the continuity of the nodal conditions of f, f', f'' and suitable end conditions (such as zero second derivative for f). Yu et al. [84] reported that it is important to maintain the spatial symmetry and high-order accuracy in the interpolation along the interface. Otherwise the numerical error in this process will cause artificial asymmetry and lead to excessive numerical viscosity.

It is noted that in addition to the spatial interpolation, there is a need for temporal interpolation on all nodes at the fine block boundary $\overline{\mathrm{MN}}$ in order to obtain quantities such as $\tilde{f}_\alpha(t^{n+1/2}, \overline{\mathrm{MN}})$. A three-point Lagrangian interpolation formula can be used [84].

3.3. Assessment of interface conservation in multi-block method

The lid-drive cavity flow has been extensively used as a benchmark solution to test the accuracy of a numerical method. In this flow, two singular points at the upper corners of the lid require high resolution to obtain satisfactory stress distribution near the corner points. To assess the accuracy of the LBE results, the benchmark solutions by Ghia et al. [105] were also used by Yu et al. [84] for direct comparisons.

The computations were carried out using (i) a single-block with uniform lattice (129×129) with the walls placed halfway between lattices, and (ii) a multi-block whose layout is shown in Fig. 10. For the multi-block case, in the two upper corner regions, the grid resolution is increased by a factor of 4 comparing with the single-block case. For $Re = 100$, the streamlines shown in Fig. 11 were obtained from the single-block solution and the pattern is not discernable from those of the

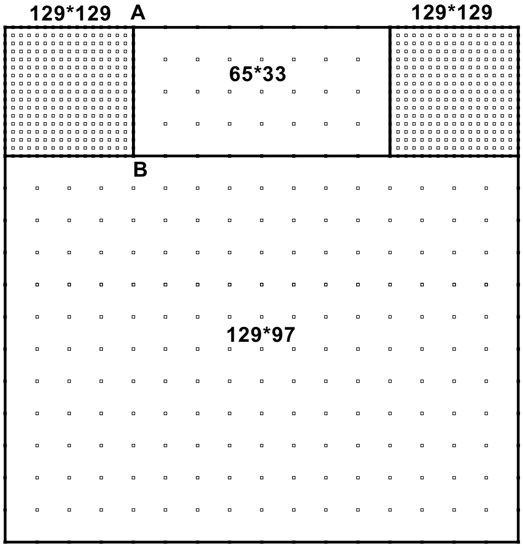

Fig. 10. Block layout for a 2-D cavity. Lattice spacing is reduced by a factor of 8 for graphical clarity [84].

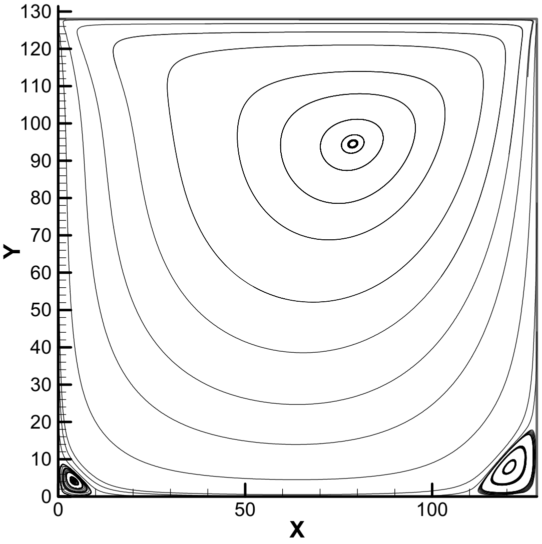

Fig. 11. Streamlines in the cavity flow at $Re = 100$ [84].

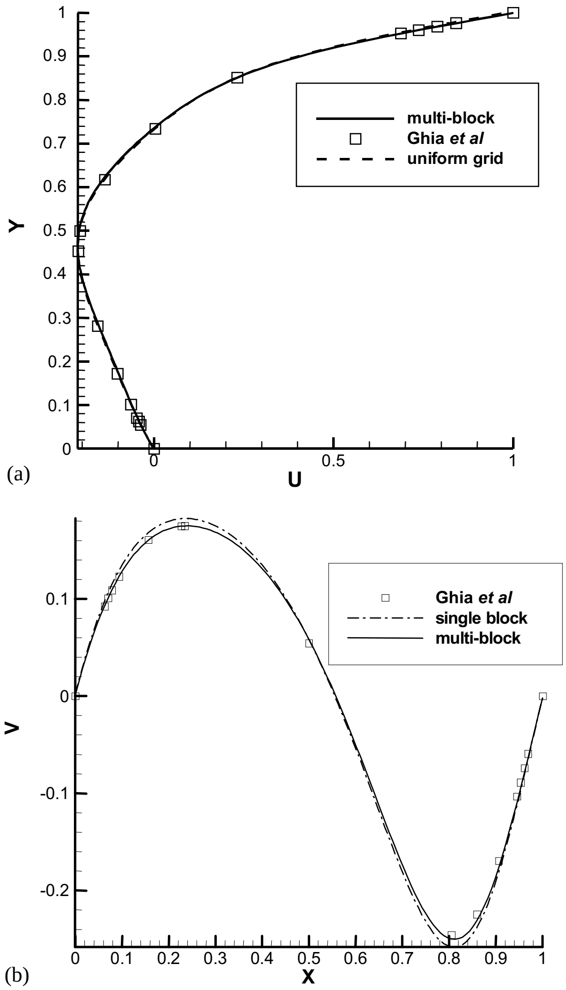

Fig. 12. Comparison of velocity between results of single-block, multi-block [84] and result of Ghia et al. [105]. (a) Comparison of u-velocity along the vertical line through geometric center and (b) comparison of v-velocity along the horizontal line through geometric center.

multi-block solution. The positions of the centers of the primary vortices are (0.6154, 0.7391) and (0.6172, 0.7390) for uniform grid and multi-block solutions, respectively, compared well with the value (0.6172, 0.7344) from Ghia et al. [105]. The u- and v-components of the velocity along the vertical line and horizontal line through the geometry center are shown in Figs. 12a and b, respectively. It is seen that while the single-block method with 129×129 lattices can capture most of physical variables satisfactorily, the multi-block method can improve the quality of the solution. Fig. 13 shows the pressure contour from the single-block computation. Because of the singularity at the upper corners, the density contours exhibit noticeable oscillations due to the insufficient resolution near singularities. Fig. 14 shows the pressure contours obtained from the multi-block solution. Significant improvement in the smoothness of the solution for the pressure field over that of the single-block solution is observed.

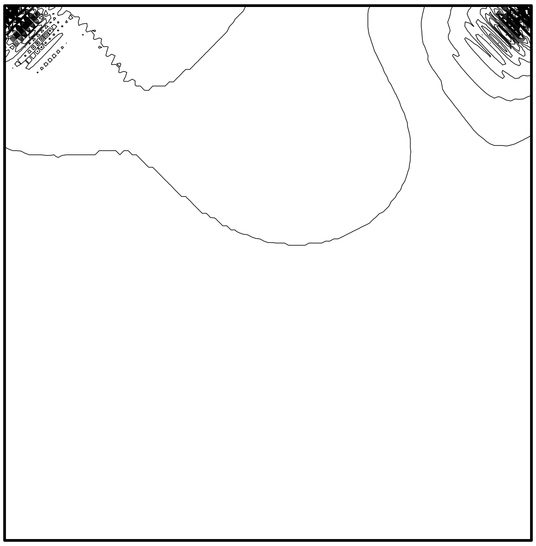

Fig. 13. Pressure contours in the cavity flow from the single-block LBE simulation [84].

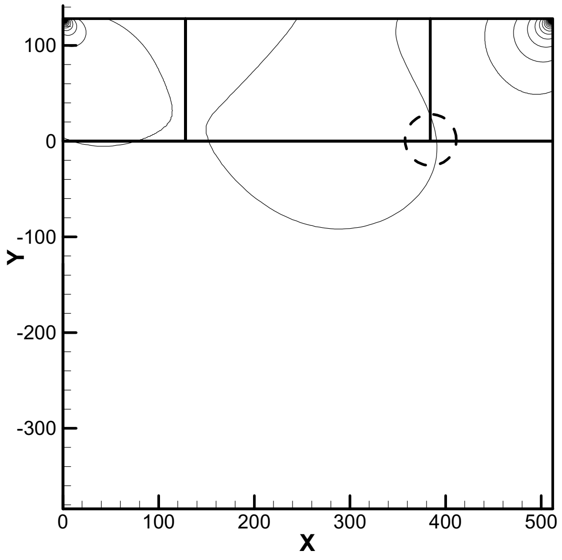

Fig. 14. Pressure contours in the cavity from multi-block LBE solution [84] (for the circled region, see Fig. 15).

In an NS solver for incompressible flows, because of the decoupling of thermodynamic pressure and velocity field, it is important to maintain the mass conservation of the entire flow domain. This issue becomes critical when the multi-block method is used [97]. Also for incompressible flows, the pressure is arbitrary up to a constant. Hence, coupling the pressure term while maintaining the mass flux conservation is very important. Generally speaking, it is difficult to maintain simultaneously the continuity of mass, momentum, and stresses across the interface between neighboring blocks because interpolations are applied to each dependent variable. In the multi-block LBE method, the continuities of mass and stresses are ensured through the use of Eqs. (25) and (26). The most important point is that interpolations are only applied to $\tilde{f}_\alpha$'s along the interface and this automatically ensures the consistency in the transfer of various flux terms across the interface.

To validate the above arguments, pressure and shear stress near the block interfaces were examined. Fig. 15 shows a local, enlarged view of the pressure contour

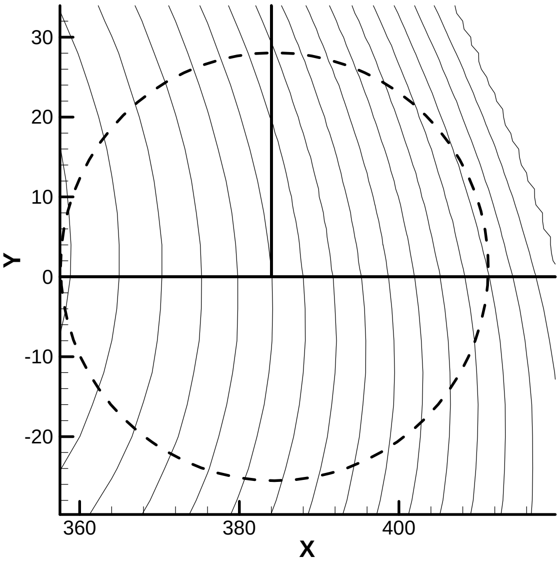

Fig. 15. Enlarged view of pressure contour in the circled region in Fig. 14 near the intersection of three blocks. The figure demonstrates that the block interface and corner are well handled [84].

around an interface corner point indicated by the circle in Fig. 14. Clearly, the pressure is smooth across the interface with the coarse-to-fine grid size ratio of $m = 4$. Fig. 16 shows the contours of shear stress. It is seen that these physical quantities are all smooth across the interface.

The NACA airfoils have been used extensively for numerical scheme evaluation. Flow fields at $Re = 500$, 1000, 2000, and 5000 were computed for NACA0012 airfoil by Yu et al. [84] with the multi-block LBE scheme. Fig. 17 shows the entire computational domain and the schematic of the multi-block arrangement. Fig. 18 compares the drag coefficient C_D between the LBE simulation and those calculated from Xfoil which is a coupled inviscid and boundary layer flow solver [106]. These two sets of results agree with each other very well for the range of Reynolds numbers investigated.

It is also noted that at $Re = 500$, the value of $C_D = 0.1761$ compared well with the results reported by Lockard et al. [107]: $C_D = 0.1762$ obtained using an NS equation-based solver, and $C_D = 0.1717$ using the Powerflow code developed by EXA Corporation, which was based on the LBE method [107]. In addition, the multi-block simulation for the symmetrical flow at $Re = 500$ gave a lift coefficient of $|C_L| < 6 \times 10^{-14}$. Lockard et al. [107] reported $C_L = 1.15 \times 10^{-7}$ using an NS equation-solver and $C_L = 2.27 \times 10^{-4}$ using EXA's Powerflow code. This indicated that the multi-block method can preserve the symmetry very well.

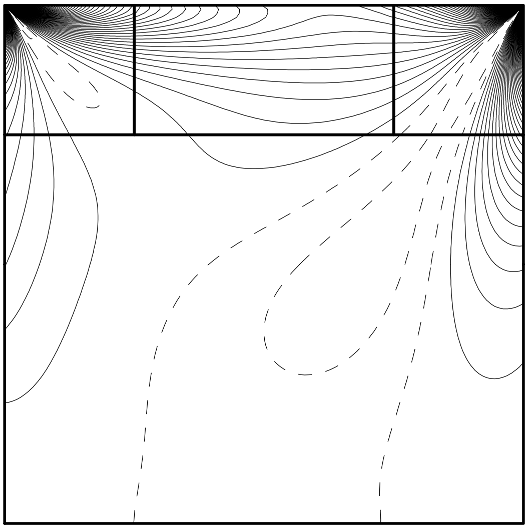

Fig. 16. Shear stress contour. Solid and dash lines represent positive and negative values, respectively [84].

It is worth pointing out that there is a significant saving in the computational cost using the multi-block method in LBE simulations. There were three different sizes of grids used for the NACA0012 airfoil simulation. There were $1025 \times 129 = 132\,225$ fine grids, 93 200 intermediate grids with $m = 4$, and 139 628 coarse grids (with $m = 8$ in reference to the finest grids) with a total of about 3.6×10^5 grids in the entire domain. If the fine grid system were used in the entire domain, the number of the grids would be $N_x \times N_y = 5698 \times 1153 \sim 6.57 \times 10^6$ which is 18 times more than

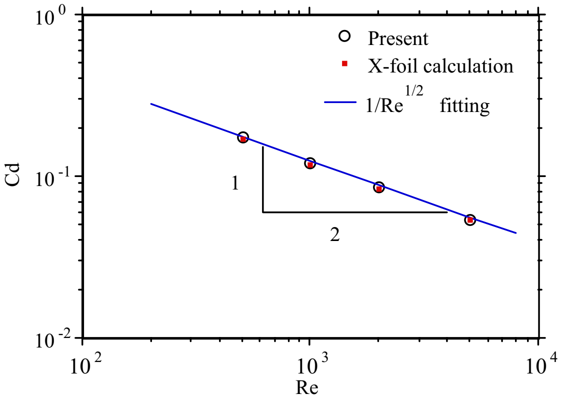

Fig. 18. Comparison of C_D between the multi-block simulation and Xfoil [106] calculation as a function of Re for flow over NACA0012 airfoil. The straight line is the slope according to the laminar boundary layer theory [84].

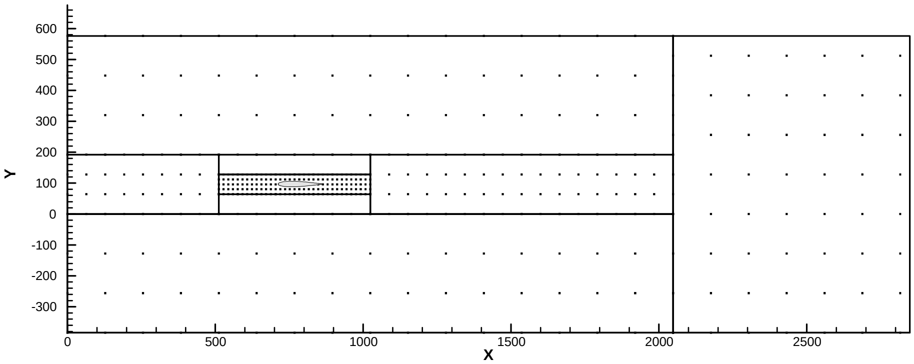

Fig. 17. Block and lattice layout for flow over NACA 0012. The lattice spacing is reduced by a factor of 32 for graphical clarity [84].

in the multi-block case. This represents a saving of 18 times in the memory. Furthermore, since $\delta t = \delta x = \delta y$ in the LBE simulation, one time step in the coarsest grid system ($m = 8$) requires two time steps in the intermediate grid blocks and eight steps in the finest grid blocks. The ratio of the computational efforts required to carry out a single-block simulations to that for a multi-block simulation for a given period of physical time would be

$$\frac{6.57 \times 10^6 \times 8}{(132\,225 \times 8 + 93\,200 \times 2 + 139\,628)} \sim 38.$$

Clearly, more saving can be achieved if more blocks of different sizes were used.

In summary, the local grid refinement and multi-block are promising methods to increase the computational efficiency of LBE method. It is important to maintain the accuracy in interface exchange of information to ensure the mass conservation and stress continuity between neighboring blocks. With efficiency aspects greatly improved, there is a significant potential for the multi-block strategy in the LBE method for practical flow problems.

4. Solid boundary treatments

Chronologically, LBE method was evolved from the LGA method [19–22]. In dealing with straight walls, the bounce-back condition was proposed in conjunction with the LGA method [108,109]. Curved walls were treated as a series of steps. This method has been extensively used in LBE simulation [85,86]. Only more recently, efforts have been made to preserve the geometric integrity [83,87–89] of the curved walls which is important in simulating high Reynolds flows.

4.1. Boundary conditions for straight walls

The bounce-back condition is very simple, efficient and easy to implement. In the standard bounce-back scheme, which is also called bounce-back at nodes scheme, the wall is placed at the lattice nodes, i.e. $\boldsymbol{x}_\mathrm{b} = \boldsymbol{x}_\mathrm{w}$ and $\Delta = 1$ in Fig. 2. However, the precise location where the flow boundary conditions are satisfied (up to 2nd order accuracy) is not at a lattice node in general [92]. This is one of major differences between the LBE method and NS solvers and it deserves attention. Ziegler [85] made an improvement to the bounce-back at node scheme. After streaming, $f_\alpha(\boldsymbol{x}_\mathrm{b})$ is known while $f_{\bar{\alpha}}(\boldsymbol{x}_\mathrm{b})$ is not. After setting $f_{\bar{\alpha}}(\boldsymbol{x}_\mathrm{b}) = f_\alpha(\boldsymbol{x}_\mathrm{b})$ on the wall (for the no-slip condition), an additional collision is then carried out at $\boldsymbol{x}_\mathrm{b}$ to yield $\tilde{f}_{\bar{\alpha}}(\boldsymbol{x}_\mathrm{b}, t)$. This additional collision was responsible for the improved accuracy. In simulating suspension flow, Ladd [53] placed the wall halfway between the nodes, which is referred to as bounce-back at link scheme. In doing so, the additional collision in Ziegler's scheme is avoided. It has been shown that this treatment has the second-order accuracy for straight walls.

Noble et al. [110] presented an improved boundary condition for 2-D hexagonal lattice. The hydrodynamic conditions, velocity and density at wall, were used to derived boundary condition for f_α's so that it can guarantee the no-slip condition. Inamuro et al. [111] and Maier et al. [112] subsequently presented similar schemes for square lattice to reduce the wall-slip velocity. Chen et al. [113] placed the wall at the lattice nodes and used extrapolation of f_α on the fluid side to obtain f_α at $\boldsymbol{x}_\mathrm{b}$. To solve f_α's which can satisfy hydrodynamic conditions at boundary nodes for D2Q9 and D2Q15 models, Zou and He [114] placed wall at nodes and extended the bounce-back scheme to the non-equilibrium part of distribution function (see Section 5 for further information). He et al. [115] proved that bounce-back on the link scheme had second-order accuracy for no-slip condition on the wall in a channel flow using an analytical solution.

All the boundary treatments mentioned above model a curved wall as zig-zag steps, which results in geometric discontinuities and affect the computational accuracy. This error worsens when *Re* increases.

4.2. Second-order accuracy models for curved walls

Filippova and Hänel [83] presented a curved boundary condition which, for the first time, provided a second-order accurate treatment for a curved solid wall. To improve the numerical stability, Mei et al. [87] presented an improved curved boundary condition based on the scheme of Filippova and Hänel. Bouzidi et al. [88] proposed a different but simple boundary condition for curved wall based on interpolation and the bounce-back scheme. Recently, Yu et al. [89] proposed a unified solid wall boundary condition based on interpolation and the balance of momentum on the wall. These four treatments for boundary conditions will be highlighted with more details on the unified solid boundary condition proposed by Yu et al. [89].

To construct $\tilde{f}_{\bar{\alpha}}(\boldsymbol{x}_\mathrm{b}, t)$ based upon known information in the surrounding fluid nodes, Filippova and Hänel [83] proposed the following linear interpolation:

$$\tilde{f}_{\bar{\alpha}}(\boldsymbol{x}_\mathrm{b}, t) = (1 - \chi)\tilde{f}_\alpha(\boldsymbol{x}_\mathrm{f}, t) + \chi f_{\bar{\alpha}}^{(*)}(\boldsymbol{x}_\mathrm{b}, t) + 2 w_{\alpha\rho} \frac{3}{c^2} \boldsymbol{e}_{\bar{\alpha}} \cdot \boldsymbol{u}_\mathrm{w} \tag{28}$$

with

$$f_\alpha^{(*)}(\boldsymbol{x}_\mathrm{b}, t) = w_{\alpha\rho}(\boldsymbol{x}_\mathrm{f}, t)\left[1 + \frac{3}{c^2}\boldsymbol{e}_\alpha \cdot \boldsymbol{u}_\mathrm{bf} + \frac{9}{2c^4}(\boldsymbol{e}_\alpha \cdot \boldsymbol{u}_\mathrm{f})^2 \boldsymbol{u}_\mathrm{f} \cdot \boldsymbol{u}_\mathrm{f}\right]. \tag{29}$$

In the above, $\boldsymbol{u}_{\rm f} \equiv \boldsymbol{u}(\boldsymbol{x}_{\rm f}, t)$ is the fluid velocity near the wall and $\boldsymbol{u}_{\rm bf}$ is to be chosen.

$$\boldsymbol{u}_{\rm bf} = (\Delta - 1)\boldsymbol{u}_{\rm f}/\Delta + \boldsymbol{u}_{\rm w}/\Delta \quad \text{and} \quad \chi = (2\Delta - 1)/\tau \quad \text{for } \Delta \geqslant 1/2, \tag{30a}$$

$$\boldsymbol{u}_{\rm bf} = \boldsymbol{u}_{\rm f} \quad \text{and} \quad \chi = \frac{(2\Delta - 1)}{(\tau - 1)} \quad \text{for } \Delta < \frac{1}{2}. \tag{30b}$$

This scheme was used in the simulation of flow over asymmetrically placed cylinder in the channel flow (see Fig. 8 for a typical result).

Mei et al. [87] suggested using different nodes to obtain $\tilde{f}_{\bar\alpha}(\boldsymbol{x}_{\rm b}, t)$ when $\Delta < 0.5$. The purpose was to improve the numerical stability over Filippova and Hänel's scheme. Thus, Eq. (30b) was replaced by

$$\boldsymbol{u}_{\rm bf} = \boldsymbol{u}_{\rm ff} \quad \text{and} \quad \chi = \frac{(2\Delta - 1)}{(\tau - 2)} \quad \text{for } \Delta < \frac{1}{2}, \tag{31}$$

where $\boldsymbol{u}_{\rm ff} = \boldsymbol{u}(\boldsymbol{x}_{\rm f} + \boldsymbol{e}_\alpha \delta t)$ is the fluid velocity at the ff node in Fig. 2.

A channel flow was used to illustrate the stability characteristics of the Filippova and Hänel's boundary condition, Eq. (30b), and the condition given by Eq. (31). As shown in Figs. 19 and 20, the stability of the boundary treatment by Mei et al. [87] was improved over the original Filippova and Hänel's scheme.

Bouzidi et al. [88] presented a simpler boundary condition based on the bounce-back for the wall located at arbitrary position. In their work, both linear scheme and the quadratic schemes were given to obtain $f_{\bar\alpha}(\boldsymbol{x}_{\rm f}, t + \delta t)$ which is equivalent to $\tilde{f}_{\bar\alpha}(\boldsymbol{x}_{\rm b}, t)$. The linear version was as follows:

$$f_{\bar\alpha}(\boldsymbol{x}_{\rm f}, t + \delta t) = \frac{1}{2\Delta}\tilde{f}_\alpha(\boldsymbol{x}_{\rm f}, t) + \frac{2\Delta - 1}{2\Delta}\tilde{f}_{\bar\alpha}(\boldsymbol{x}_{\rm f}, t) \quad \text{for } \Delta > \frac{1}{2}, \tag{32a}$$

$$f_{\bar\alpha}(\boldsymbol{x}_{\rm f}, t + \delta t) = 2\Delta\tilde{f}_\alpha(\boldsymbol{x}_{\rm f}, t) + (1 - 2\Delta)\tilde{f}_\alpha(\boldsymbol{x}_{\rm f}, -\boldsymbol{e}_\alpha \delta t, t) \quad \text{for } \Delta < \frac{1}{2}. \tag{32b}$$

In the above, we note that $x_{\rm f} - \boldsymbol{e}_\alpha \delta t$ is at the ff node in Fig. 2. They computed flow over a 2-D periodical array of cylinders and reported the second-order convergent results for the inverse of the permeability, Q, shown in Fig. 21.

The above three boundary condition treatments all have second-order accuracy for curved boundary. The difference is that the first two need to construct a fictitious fluid point inside the solid wall, and perform a collision step at that node, while the scheme of Bouzidi et al. only requires the known values of f_α on the fluid side and no additional collision is required. It is

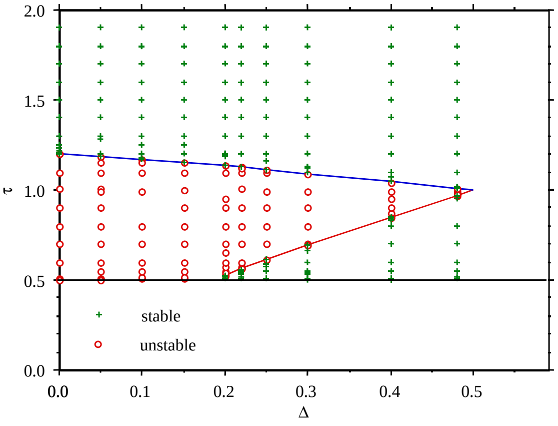

Fig. 19. Regions of stability and instability in the LBE computation for fully developed 2-D channel flow using Filippova and Hänel's boundary condition [83], for $\Delta < \frac{1}{2}$ [87].

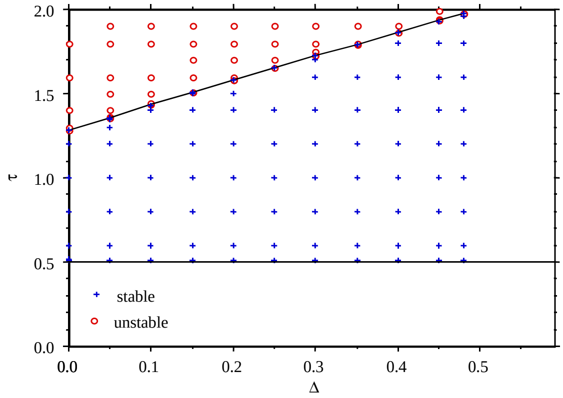

Fig. 20. Regions of stability and instability in the LBE computation for fully developed 2-D channel flow using the boundary condition of Mei et al. [87], for $\Delta < \frac{1}{2}$.

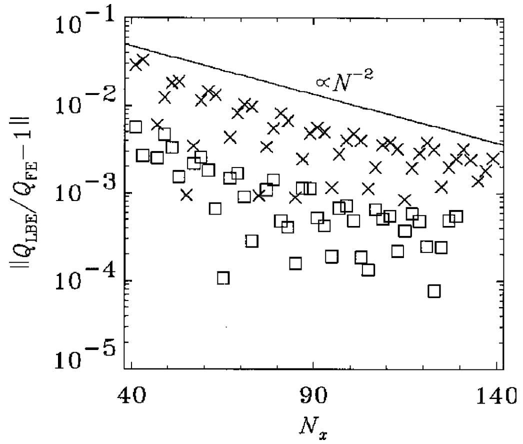

Fig. 21. Convergence of the factor Q computed by LBE with Bouzidi et al.'s quadratic (□) and linear interpolation (×) vs. computational domain size. In the simulation, the fraction of volume occupied by cylinders is kept constant [88]. Courtesy of P. Lallemand.

emphasized that all three methods need to treat the boundary condition separately for $\Delta \leqslant 0.5$ and $\Delta > 0.5$.

In the scheme by Yu et al. [89], a single interpolation was used for both $\Delta \leqslant 0.5$ and $\Delta > 0.5$ Referring to Fig. 2, after the streaming step, $f_{\bar{\alpha}}(\boldsymbol{x}_f, t+\delta t)$ for ($\bar{\alpha} = 4$ in this example) is needed while $f_\alpha(\boldsymbol{x}_b, t+\delta t)$ and $f_\alpha(\boldsymbol{x}_f, t+\delta t)$ are known. Using a linear interpolation, $f_\alpha(\boldsymbol{x}_w, t+\delta t)$ (for $\alpha = 8$) can be easily found as

$$f_\alpha(\boldsymbol{x}_w, t+\delta t) = f_\alpha(\boldsymbol{x}_f, t+\delta t) + \Delta[f_\alpha(\boldsymbol{x}_b, t+\delta t) - f_\alpha(\boldsymbol{x}_f, t+\delta t)]. \tag{33}$$

To ensure the no-slip condition ($\boldsymbol{u}_w = 0$) on the wall, considering the momentum balance in the direction of $\boldsymbol{e}_\alpha$, we set

$$f_{\bar{\alpha}}(\boldsymbol{x}_w, t+\delta t) = f_\alpha(\boldsymbol{x}_w, t+\delta t). \tag{34}$$

Using $f_{\bar{\alpha}}(\boldsymbol{x}_w, t+\delta t)$ and $f_{\bar{\alpha}}(\boldsymbol{x}_f + \boldsymbol{e}_{\bar{\alpha}}, t+\delta t)$, $f_\alpha(\boldsymbol{x}_f, t+\delta t)$ can be obtained using a linear interpolation:

$$f_{\bar{\alpha}}(\boldsymbol{x}_f) = f_{\bar{\alpha}}(\boldsymbol{x}_w) + \frac{\Delta}{1+\Delta}[f_{\bar{\alpha}}(\boldsymbol{x}_f + \boldsymbol{e}_{\bar{\alpha}}) - f_{\bar{\alpha}}(\boldsymbol{x}_w)]. \tag{35}$$

This simple, unified formula for the boundary condition is valid for both $\Delta \geqslant 0.5$ and $\Delta < 0.5$. One can easily extend the above linear formula to a quadratic or higher-order scheme using a higher-order interpolation.

For non-zero wall velocity $\boldsymbol{u}_w$, it can be easily incorporated into the unified formulation by adding an additional momentum to $f_{\bar{\alpha}}(\boldsymbol{x}_w, t+\delta t)$ given in Eq. (34) as

$$f_{\bar{\alpha}}(\boldsymbol{x}_w, t+\delta t) = f_\alpha(\boldsymbol{x}_w, t+\delta t) + 2w_\alpha \rho_w \frac{3}{c^2}\boldsymbol{e}_\alpha \cdot \boldsymbol{u}_w, \tag{36}$$

where ρ_w is the fluid density at the wall which can be obtained by using suitable extrapolation from the nearby fluid nodes. To avoid computational instability, we simply set $\rho = \rho(x_f)$ since we are dealing with nearly incompressible flows.

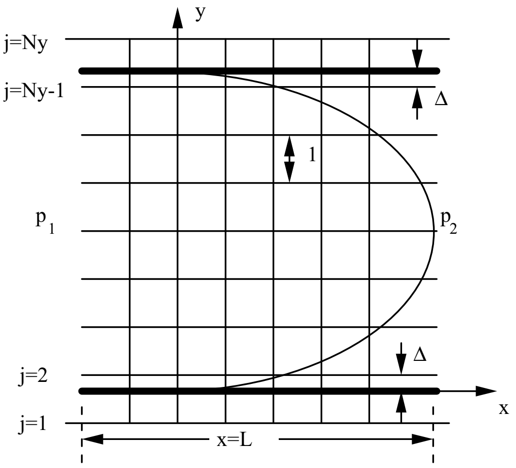

Fig. 22. Lattice distribution in channel flow simulations with arbitrary Δ.

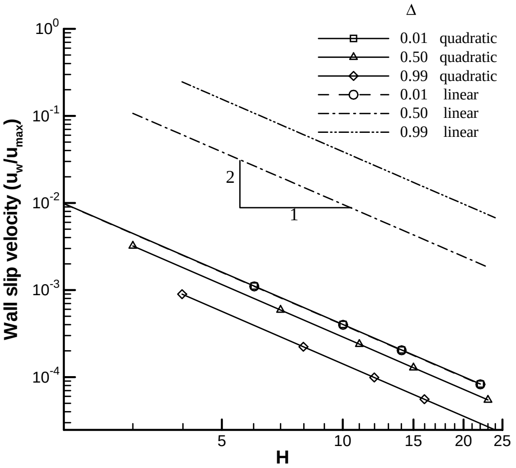

Fig. 23. Quadratic convergence of the wall-slip velocity using the boundary conditions of Yu et al. [89] in constant pressure-driven channel flow.

A Poiseuille flow (see Fig. 22) was used to illustrate the accuracy of the scheme by Yu et al. [89]. This flow is driven by a body force acting as a constant pressure gradient ∇p along the $x-$direction [115]. To assess the computational error of the LBE solution of the velocity, $u_{\mathrm{LBE}}(y)$, the following relative L_2-norm error is defined:

$$E_2 = \frac{\left\{\int_0^H [u_{\mathrm{LBE}}(y) - u_{\mathrm{exact}}(y)]^2\, \mathrm{d}y\right\}^{1/2}}{\left[\int_0^H u_{\mathrm{exact}}^2(y)\mathrm{d}y\right]^{1/2}}. \tag{37}$$

The periodic boundary condition for f_α's was used at the left and right boundaries of the computational domain. At the lower and upper walls, three wall boundary conditions were used: (i) Filippova and Hänel's method, (ii) the method of Bouzidi et al., and (iii) the method of Yu et al. given by Eq. (35).

The wall-slip velocity $u_w = u_x(y=0)$ is evaluated using a second-order extrapolation based on $u_x(y=\Delta)$, $u_x(y = 1+\Delta)$ and $u_x(y = 2+\Delta)$. Here it is supposed that the velocity profile of the solution is parabolic so that this second-order extrapolation is adequate. Since the true wall velocity in the pressure-driven channel flow is exactly zero, the wall-slip velocity u_w provides a measure of the accuracy for the treatment of the wall velocity. Fig. 23 shows the dependence of wall-slip velocity to the H (or the grid resolution H^{-1}). Here u_w is normalized by the centerline velocity

$$u_{\max} = -\frac{H^2}{8\rho\nu}\frac{\mathrm{d}p}{\mathrm{d}x}. \tag{38}$$

The second-order convergence of u_w with increasing H is observed clearly in Fig. 23 for $\Delta = 0.01$, 0.5, and 0.99. It is worth noting that the magnitude of error of

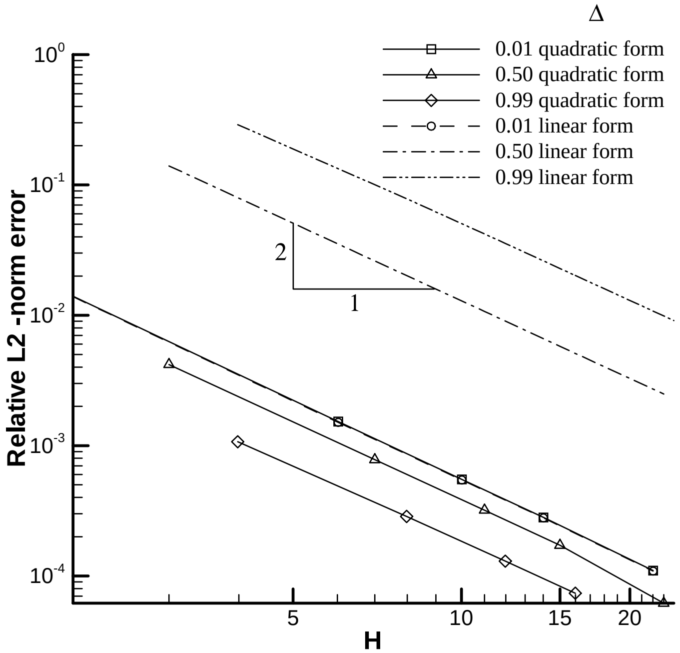

Fig. 24. Dependence of relative L_2-norm error for the boundary conditions of Yu et al. [89] on the lattice resolution H in steady-state pressure-driven channel flow simulations.

the quadratic form given by Yu et al. [89] is much smaller.

Fig. 24 shows the dependence of the relative L_2-norm error on the channel height H for $\Delta = 0.01, 0.5$, and 0.99 for the method of Yu et al. [89]. The second-order accuracy is clearly demonstrated in the range of H investigated.

While the wall-slip velocity u_w can be viewed as an error in the approximate treatment for the boundary condition for the distribution function, it can also be viewed as resulting from the error in locating the wall in the LBE solution. As shown in Fig. 22, the bottom wall is supposed to be at a distance of Δ below the $j = 2$ grid line. The LBE solution, however, sees the wall at a distance of Δ' below the $j = 2$ grid. Using a third-order polynomial and the velocity values at $j = 2$, 3, 4 and 5 to fit the velocity profile near the wall, it is found that the coefficient for the cubic power term is 0; hence, a parabolic profile is an exact fit. Using the parabolic fit, the wall position Δ' can be determined. The difference $(\Delta' - \Delta)$ can be used as a measure of geometric accuracy in the LBE solution. Fig. 25 shows the $(\Delta' - \Delta)$ as a function of $1/H$ for $\Delta = 0.01$, 0.5, and 0.99 using the present linear scheme. Although graphically not obvious, $(\Delta' - \Delta) \sim -1/100H^{-1}$ for $\Delta = 0.01$. Hence, $(\Delta' - \Delta)$ is proportional to H^{-1} to the leading order. This asymptotic linear relationship holds also for other values of τ. With the linear scheme of Bouzidi et al., the linear relationship is also observed and the results for $\tau = 0.51$ are very close to that shown in Fig. 25. Hence, the non-dimensional geometric error scales with H^{-2} and $H'(\Delta' - \Delta)$ remains a constant.

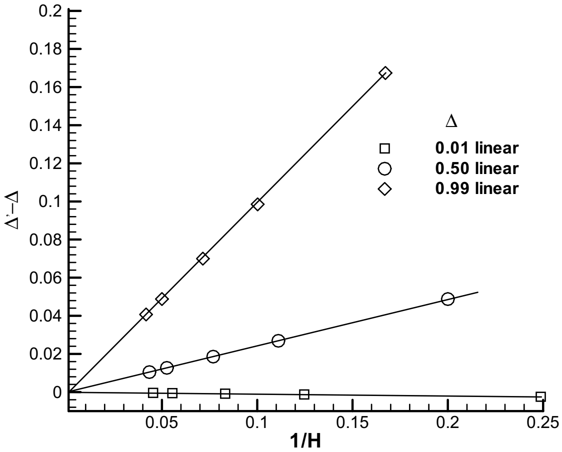

Fig. 25. Variation of $(\Delta' - \Delta)$ as a function of $1/H$ for $\Delta = 0.01$, 0.5, and 0.99 using the linear scheme of Yu et al. [89].

As the wall location is altered, the channel height is also modified to $H' = H + 2(\Delta' - \Delta)$. Thus, the LBE solution actually sets up the following parabolic velocity profile:

$$u'_{\text{exact}}(y') = -\frac{1}{2\rho\nu}\frac{\mathrm{d}p}{\mathrm{d}x}(y'^2 - H'y'). \tag{39}$$

It is thus instructive to compare the LBE solution with the above modified exact velocity profile using the following L_2-norm error,

$$\mathrm{E}'_2 = \frac{1}{H'}\left\{\int_0^{H'}[u_{\mathrm{LBE}}(y) - u'_{\text{exact}}(y')]^2\,\mathrm{d}y'\right\}^{1/2}. \tag{40}$$

Fig. 26 shows E'_2 as a function of H for $\Delta = 0.01$, 0.5, and 0.99. Basically, E'_2 has reached the machine error.

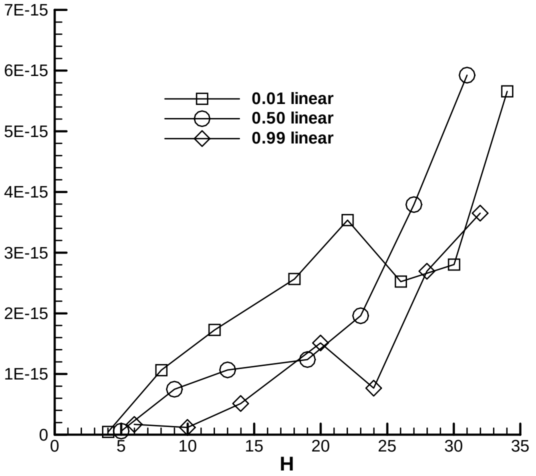

Fig. 26. Dependence of relative L_2-norm error, defined in Eq. (40), on the lattice resolution H using the linear scheme of Yu et al. [89] in the steady-state pressure-driven channel flow.

With the modified exact velocity profile $u'_{\text{exact}}(y')$, the slip velocity can be calculated as

$$u_{\mathrm{w}} \sim u'_{\text{exact}}(y' = \Delta' - \Delta) = \frac{1}{2\rho\nu}\frac{\mathrm{d}p}{\mathrm{d}x}\left[H'(\Delta' - \Delta) - (\Delta' - \Delta)^2\right]. \tag{41}$$

Closer examination of the actual values of u_{w} as a function of H reveals that, for a given set of $(\tau, \mathrm{d}p/\mathrm{d}x, \Delta)$, u_{w} does not vary with H. Hence,

$$u_{\mathrm{w}} = \frac{1}{2\rho\nu}\frac{\mathrm{d}p}{\mathrm{d}x}B, \tag{42}$$

where the coefficient B is a function of $(\tau, \mathrm{d}p/\mathrm{d}x, \Delta)$. This makes the presentation for the slip velocity much easier since one set of H is sufficient. Fig. 27 shows the slip wall velocity as a function of Δ using Yu et al.'s linear scheme and Bouzidi et al.'s linear scheme for $\tau = 0.502$, 0.51, 0.6 and 0.8 while the value of $(1/\nu)(\mathrm{d}p/\mathrm{d}x)$ is fixed. The linear version of these two schemes have very similar characteristics in terms of accuracy.

It is further noticed that the largest magnitude of the slip velocity occurs mainly near $\Delta = 1$. This can be attributed to the fact that the interpolation formula given by Eq. (35) has the largest error at $\Delta = 1$. Thus to reduce the wall-slip velocity, the second-order interpolation formula may be used [89]. Fig. 28 shows the wall-slip velocity as a function of Δ using both quadratic forms of Yu et al.'s scheme and Bouzidi et al.'s scheme for $\tau = 0.502$, 0.51 and 0.6. Note that for the quadratic scheme of Yu et al., the slip velocity is amplified by a factor of 100 for $\tau = 0.502$ and by a factor of 10 for $\tau = 0.51$ in order to show all curves on the same scale. For the low viscosity ($\tau = 0.502$) case, the slip velocity using Bouzidi et al.'s quadratic scheme is over 100 times of that using the quadratic formula of Yu et al.

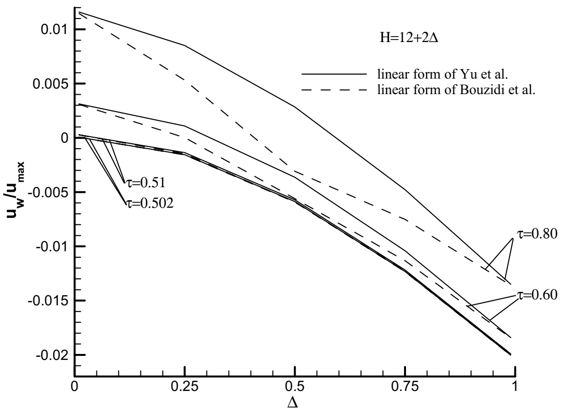

Fig. 27. Slip wall velocity as a function of Δ using the linear scheme of Yu et al. [89] and Bouzidi et al.'s [88] linear scheme for $\tau = 0.502$, 0.51, 0.6 and 0.8. The value of $(1/\nu)(\mathrm{d}p/\mathrm{d}x)$ is fixed.

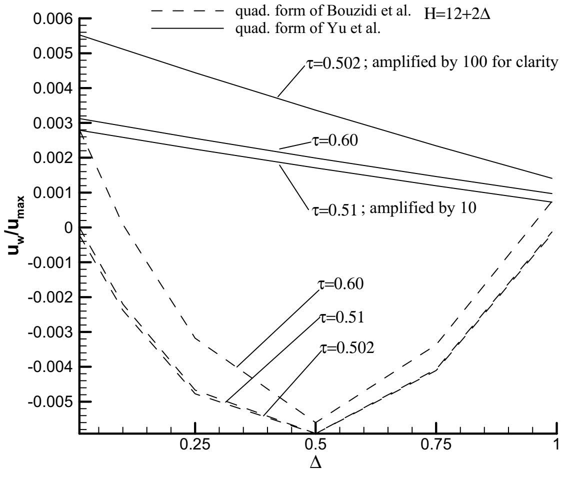

Fig. 28. Slip wall velocity as a function of Δ using the quadratic scheme of Yu et al. and Bouzidi et al. [88] for $\tau = 0.502$, 0.51, 0.6 and 0.8. The value of $(1/\nu)(\mathrm{d}p/\mathrm{d}x)$ is fixed.

However, it also needs to be pointed out that for $\tau \geqslant 0.6$, not only these two quadratic schemes perform very similarly, but also there is little difference between the linear and quadratic versions of the both Bouzidi et al.'s and Yu et al.'s schemes. Since the high Reynolds number flow is more difficult to obtain computationally, it is important to realize that quadratic form of the Yu et al.'s scheme may result in a much larger improvement in handling the solid boundary conditions for the large eddy type of LBE simulations.

Fig. 29 shows the relative error defined by Eq. (37) as a function of Δ using the method of Yu et al., Filippova and Hänel's method, and method of Bouzidi et al., for $0 \leqslant \Delta \leqslant 1$. In simulation $\tau = 0.51$ and $\nabla p = -10^{-8}$. It can be seen that the linear scheme of Yu et al., linear scheme of Bouzidi et al., and Filippova and Hänel's boundary condition have the same order of error for $0 \leqslant \Delta \leqslant 1$. Bouzidi et al.'s quadratic form gives a large range of error for $0 \leqslant \Delta \leqslant 1$, from 10^{-7} to 10^{-2}. The quadratic formula of Yu et al. yields a more uniformly distributed error in the whole range of Δ. This observation agrees well with the one obtained by analyzing of wall-slip velocity. It is interesting to note that the error goes down when Δ increase for the quadratic formula of Yu et al., which is opposite to the trends shown in other boundary treatments. The linear form of Yu et al. and the linear form of Bouzidi et al. have very similar characteristics. Unlike the Filippova and Hänel's boundary condition, the boundary conditions of Yu et al. and Bouzidi et al. suffer from no computational instability for τ near 0.5; it can also handle any value of Δ between 0 and 1. Even for $\tau = 0.5001$, these two schemes give a correct, converged result.

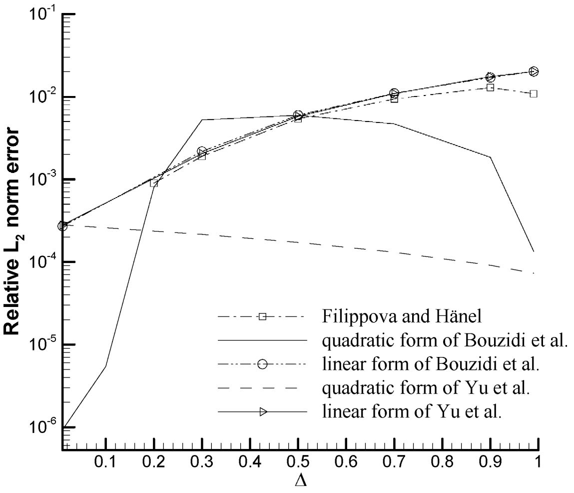

Fig. 29. Relative L_2-norm error as a function of Δ for boundary conditions of Filippova and Hänel [83], Bouzidi et al. [88], and Yu et al. [89] in steady-state pressure-driven channel flow simulations. $H = 12 + 2\Delta$ in the simulation [89].

Table 1
Comparison of drag coefficient using three boundary treatments

X	Linear form of Yu et al.	Quadratic form of Yu et al.	Filippova and Hänel's scheme	C_D (Fornberg [100])
130.0	1.275	1.247	1.271	1.248
130.2	1.290	1.251	1.274	

A uniform flow over a column of circular cylinders was simulated by Yu et al. [89] to evaluate the performance of the unified boundary treatment along with Filippova and Hänel's boundary condition on curved boundary. Reynolds number is 100 based on the diameter of the cylinder and inlet velocity. The drag coefficient was calculated using the momentum exchange method for both boundary treatments with two different cylinder center positions: $(x_c, y_c) = (130.0, 65.0)$ and (130.2, 65.0) lattice unit. Different positions of the cylinder center give different values of Δ.

Table 1 shows the results of drag coefficient using the Filippova and Hänel's method, the linear, and the quadratic formulae of Yu et al. The quadratic formula of Yu et al. gives a closer value in comparison with the value of 1.248 given by Fornberg [100] for both cylinder positions.

Flow over an oscillating flat plate at $Re = 20$ was calculated to examine the performance of boundary treatments when solid boundary crossed the middle of nodes (i.e. Δ changes from less than 0.5 to larger than 0.5). To avoid the crossing of the plate through lattice nodes, the plate is moved according to

$$y_{\text{plate}} = y_{\text{initial}} + 0.49\sin(t/1000)$$

with y_{initial} set to be at the middle of the nodes ($\Delta = 0.5$). Filippova and Hänel's method, linear scheme of Bouzidi et al. and linear scheme of Yu et al. were used on the surface of the plate. Figs. 30a and b show the variation of drag as the plate moves up and down. There is a small discontinuity in the results using the schemes of Filippova and Hänel, and Bouzidi et al. when the plate crosses $y = y_{\text{initial}}$. On the other hand, the unified scheme of Yu et al. gives a result with a smooth temporal variation.

In summary, recent development of boundary conditions on curved solid wall in LBE is reviewed. Starting from the work of Filippova and Hänel [83], the geometric integrity in LBE has been accurately maintained. The scheme proposed by Bouzidi et al. [88] preserved the original physical idea of the bounce-back scheme, achieved second-order accuracy, and simplified the calculation. The unified scheme developed by Yu et al. [89] further simplified the calculation, eliminated the discontinuity in the boundary treatment. Both

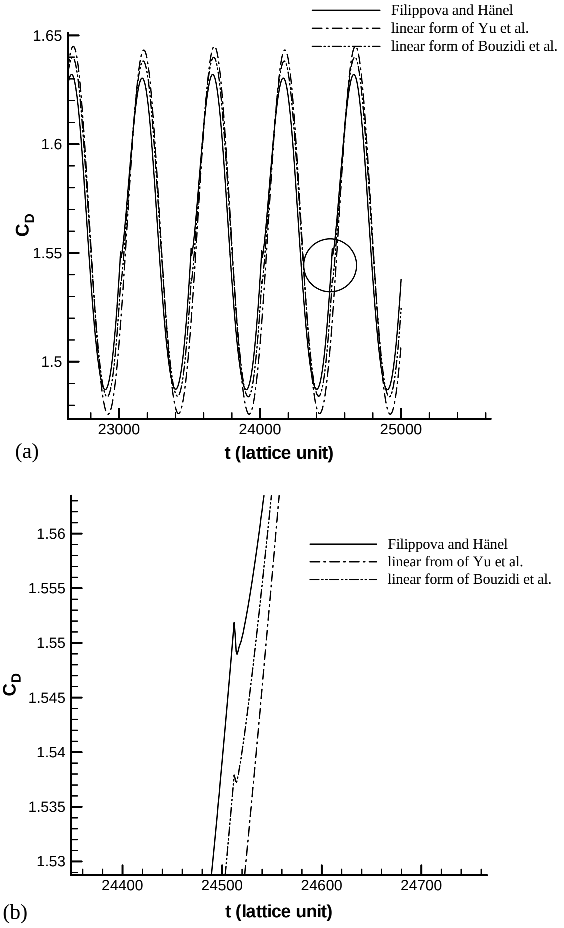

Fig. 30. (a) Drag coefficient C_D for flow over oscillating zero-thickness flat plate using three different boundary conditions: Filippova and Hänel [83], Bouzidi et al. linear [88], and linear scheme of Yu et al. [89]. (b) Enlarged view of C_D in the circled region in Fig. 30a when Δ changes from less than 0.5 to larger than 0.5. The figure demonstrates the discontinuity in the temporal variation caused by the Filippova and Hänel [83] and Bouzidi et al.'s boundary treatment [88].

Bouzidi et al.'s and Yu et al.'s schemes are robust and have good computational stability characteristics.

5. Inlet boundary treatments and their effects on computational stability

Open boundaries refer to lines (or planes) of symmetry, periodic boundary, inlet and outlet. For simplicity, the far field boundary where free stream velocity is specified is also grouped with the inlet boundary. On the symmetric and periodic boundaries, the conditions for f_α's can be assigned without ambiguity. At the outlet of a computational domain, the f_α's can usually be approximated by a simple extrapolation. In general, the boundary treatments for solid wall have been directly extended to the inlet boundary with known velocity to provide the required inlet condition for f_α's [90,85,91,114]. However, little attention has been paid to the effect of the interaction between the inlet boundary and the interior of the flow field on stability of the computation and the quality of the solution.

5.1. Interaction between inlet boundary and interior flow field

Let us consider a horizontal flow at an inlet (Fig. 31). The first vertical grid line is at $\mathbf{x}_A$. The inlet is located at $\mathbf{x}_I$ which is between node A at $\mathbf{x}_A$ and node B at $\mathbf{x}_B$. The node B is the first fluid node next to the inlet. Using the bounce-back on the link scheme, one typically requires that the known velocity profile $\mathbf{u}(\mathbf{x}_I)$ be specified at $\mathbf{x}_A + \frac{1}{2}\mathbf{e}_1\delta t$ with $\Delta = 0.5$. The standard bounce-back scheme for $\tilde{f}_{\bar\alpha}(\mathbf{x}_A)$ at the inlet $\mathbf{x}_A$ gives

$$\tilde{f}_{\bar\alpha}(\mathbf{x}_A) = \tilde{f}_\alpha(\mathbf{x}_A + \mathbf{e}_{\bar\alpha}\delta t) + 2w_\alpha\rho\left(\mathbf{x}_A + \frac{1}{2}\mathbf{e}_{\bar\alpha}\delta t\right)\frac{3}{c^2}\mathbf{e}_{\bar\alpha}\cdot\mathbf{u}(x_I) \qquad (43)$$

for $\bar\alpha = 1,2,8$ and $\alpha = 5,6,4$. We note that $\tilde{f}_{\bar\alpha}(\mathbf{x}_A)$ in Eq. (43) completely depends on $\tilde{f}_\alpha(\mathbf{x}_A + \mathbf{e}_{\bar\alpha}\delta t)$ and

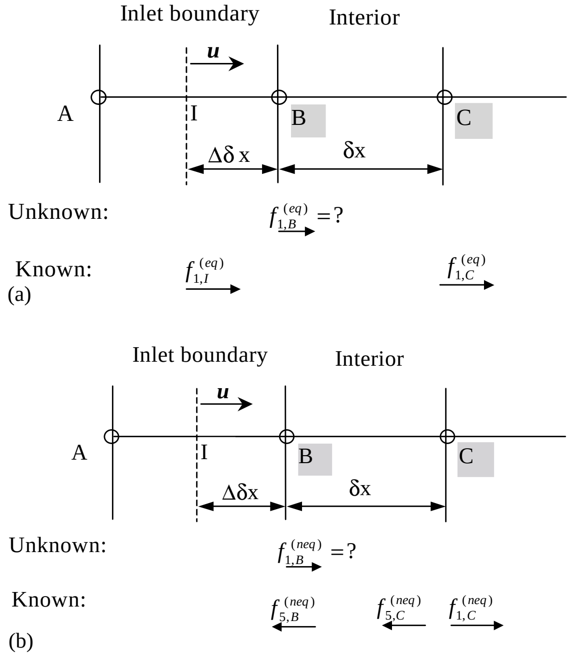

Fig. 31. Configuration of distribution functions which are used to construct inlet boundary condition. (a) Schematic for determining the equilibrium distribution at the inlet and (b) schematic for determining the non-equilibrium distribution at the inlet.

$\rho(\boldsymbol{x}_A + \frac{1}{2}\boldsymbol{e}_{\bar{\alpha}}\delta t)$ which are in the interior of flow field. Thus, it creates a mechanism for the pressure waves to propagate along the $\boldsymbol{e}_\alpha$ direction through $\tilde{f}_\alpha(\boldsymbol{x}_A + \boldsymbol{e}_{\bar{\alpha}}\delta t)$ and to reflect back to the interior of computational domain along the $\boldsymbol{e}_{\bar{\alpha}}$ direction through $\tilde{f}_{\bar{\alpha}}(\boldsymbol{x}_A)$.

To demonstrate how the pressure wave in the interior of the computational domain interact with the inlet boundary when the bounce-back scheme is used, Yu [116] considered a uniform flow of velocity u over a column of circular cylinder at $Re = 500$ as shown in Fig. 32. At $t = 0$, a simple uniform flow was specified as initial condition. Hence, both shear waves and normal waves are generated near the cylinder surface for $t > 0$.

To detect the impact of the pressure waves on the inlet boundary, the pressure at a selected monitoring point M was continuously monitored as a function of time. The monitoring point M is located on the centerline and about 20 lattices from the inlet and about 109 lattices from the front stagnation point of the cylinder. Fig. 33 shows $P_M(t)$ which is the variation of pressure at point M from the start of the computation. Owing to the uniform flow initial condition, discontinuity in macroscopic variables (p and $\boldsymbol{u}$) is introduced at $t = 0$ on the surface of the cylinder. Thus, the spurious pressure wave will propagate throughout the entire flow field from the cylinder. At point M, the earliest time that one can detect the pressure wave associated with the initial discontinuity is determined by the distance from the front stagnation point of the cylinder to point M divided by the speed of sound. That is,

$$t_1 = 109\sqrt{3} \approx 189 \quad \text{(lattice unit).}$$

It is seen in Fig. 33 that indeed that first impulse of the pressure wave at point M occurs near $t \approx 189$. This confirms the forgoing analysis on the nature of the pressure wave propagation. And such transient variation for $t < t_1$ is completely independent of the choice of the inlet boundary conditions.

Proceeding with the above analysis, it is easily seen that this initial pressure pulse will continue to move toward left and hit the inlet boundary at $t = (109 + 20)\sqrt{3} \approx 224$ (lattice unit). Because of the expected interaction with the inlet boundary under the standard bounce-back condition, this pressure wave will be partially reflected back to the interior of the flow field. At the speed of sound c_s, this pressure wave will again pass point M at

$$t_2 = (109 + 20 + 20)\sqrt{3} \approx 258 \text{ (lattice unit).}$$

It is seen that in Fig. 33 that the second peak in the $P_M(t)$ curve occurs at $t_2 \approx 258$. It is also noted that the peaks of the $P_M(t)$ at $t = t_1$ and t_2 do not differ substantially. This implies that the standard bounce-back treatment reflected back most of the disturbance.

Grunau [117] placed the inlet at the lattice node $\boldsymbol{x}_A$ ($\boldsymbol{x}_I = \boldsymbol{x}_A$ and $\Delta = 1$) as opposed to the lattice halfway link between the grids in which $\Delta = 0.5$ as shown in

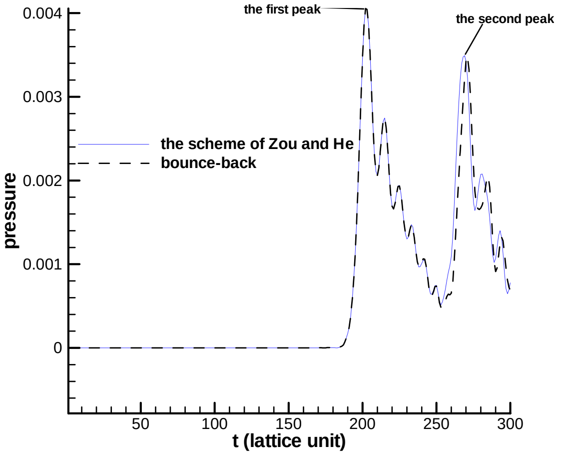

Fig. 33. Pressure variation $(\rho - 1)/3$ at point M at the beginning stage of computation by using the bounce-back inlet condition. Uniform velocity is given as initial condition [116].

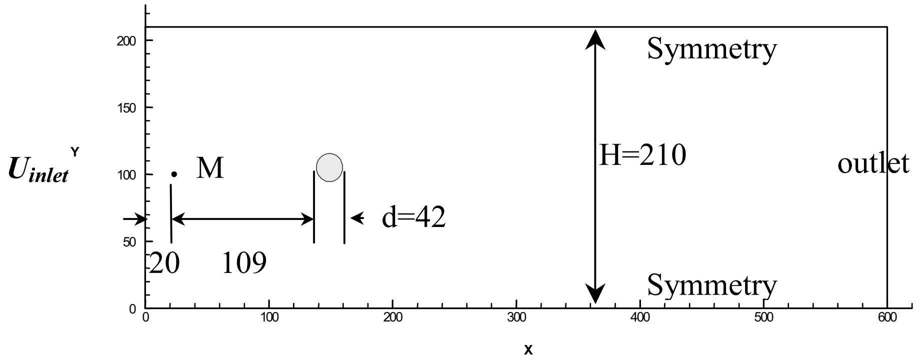

Fig. 32. Computational domain and boundary conditions.

Fig. 31. He then assigned the equilibrium distribution function to be the desired $\tilde{f}_{\bar{\alpha}}(\boldsymbol{x}_A)$ at the inlet. For the D2Q9 model, this method gives

$$\tilde{f}_{\bar{\alpha}}(\boldsymbol{x}_A) = f_{\bar{\alpha}}^{(\mathrm{eq})}(\boldsymbol{x}_A) = w_{\bar{\alpha}}\rho(\boldsymbol{x}_I)\left[1 + \frac{3}{c^2}\boldsymbol{e}_{\bar{\alpha}} \cdot \boldsymbol{u}(\boldsymbol{x}_I) + \frac{9}{2c^4}(\boldsymbol{e}_{\bar{\alpha}} \cdot \boldsymbol{u}(\boldsymbol{x}_I))^2 - \frac{3}{2c^2}\boldsymbol{u}^2(\boldsymbol{x}_I)\right] \quad (44)$$

for $\bar{\alpha} = 1, 2$, and 8. Zou and He [114] pointed out that this method has a larger error than the one using Eq. (43).

Skordos [118] presented a scheme to calculate f_α from a given initial velocity and density field. In his scheme the boundary was placed at the lattice nodes ($\boldsymbol{x}_I = \boldsymbol{x}_A$) in Fig. 31 and the first-order term in the Chapman–Enskog expansion, $f^{(1)}$, is added to $f^{(\mathrm{eq})}$ to obtain an approximate distribution function,

$$f_{\bar{\alpha}}(\boldsymbol{x}_A) = f_{\bar{\alpha}}^{(\mathrm{eq})}(\boldsymbol{x}_A) + f_{\bar{\alpha}}^{(1)}(\boldsymbol{x}_A). \quad (45)$$

In this scheme, a collision step is needed to obtain $\tilde{f}_{\bar{\alpha}}(\boldsymbol{x}_A)$. In computing $f^{(1)}$, the gradients of velocity and density are required. This method can lead to stable computation if the exact value for the velocity derivatives at the inlet instead of the finite difference is used. This is expected since such an exact treatment does not allow for interaction between the inlet boundary and the interior of the flow field. However, this results in over-specification of the boundary conditions (for macroscopic variables) as one needs both the value and derivative of the variable on one side of the domain. When the finite difference scheme is used to evaluate the derivatives, error is greatly increased and instability often develops. This approach is thus not practical.

Zou and He [114] proposed a method to specify the inlet boundary condition based on the idea of bounce-back of the non-equilibrium distribution. In this treatment, the inlet is at nodes ($\boldsymbol{x}_I = \boldsymbol{x}_A$ in Fig. 31a). For the D2Q9 model at node $\boldsymbol{x}_A$, (Fig. 34), after the streaming step, $f_0, f_3, f_4, f_5, f_6, f_7$ are known and f_1, f_2, f_8 can be determined as follows:

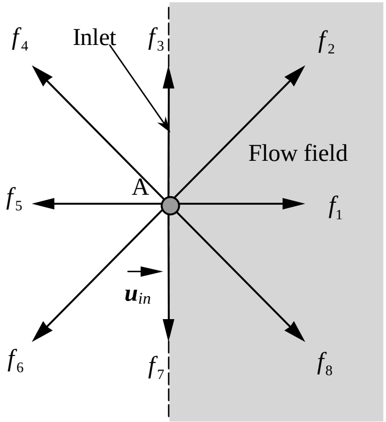

Fig. 34. Schematics of distribution function at inlet for Zou and He's method [114] at an inlet, where$f_0, f_3, f_4, f_5, f_6, f_7$ are known and f_1, f_2, f_8 are to be determined.

$$\rho(x_A) = \frac{1}{1 - u_x(\boldsymbol{x}_A)}[f_0 + f_3 + f_7 + 2(f_4 + f_5 + f_6)], \quad (46)$$

$$f_1 = f_5 + \tfrac{2}{3}\rho(\boldsymbol{x}_A)u_x(\boldsymbol{x}_A), \quad (47)$$

$$f_2 = f_6 - \tfrac{1}{2}(f_3 - f_7) + \tfrac{1}{2}\rho(\boldsymbol{x}_A)u_y(\boldsymbol{x}_A) + \tfrac{1}{6}\rho(\boldsymbol{x}_A)u_x(\boldsymbol{x}_A), \quad (48)$$

$$f_8 = f_4 + \tfrac{1}{2}(f_3 - f_7) - \tfrac{1}{2}\rho(\boldsymbol{x}_A)u_y(\boldsymbol{x}_A) + \tfrac{1}{6}\rho(\boldsymbol{x}_A)u_x(\boldsymbol{x}_A). \quad (49)$$

A collision step is needed to obtain $\tilde{f}_{\bar{\alpha}}(\boldsymbol{x}_A)$ for $\bar{\alpha} = 1, 2$, and 8.

Yu [116] applied the condition of Zou and He [114] to the problem of flow over a column of cylinders. Nearly the same pressure curve was detected at point M as the one using bounce-back scheme as shown in Fig. 33. The magnitude of second peak using the standard bounce-back and scheme of Zou and He differs only by 2%.

To recapitulate, in Eq. (43), f_α at the inlet is determined using the values of f's inside the computational domain. Hence,

$$\tilde{f}_{\bar{\alpha}}(\boldsymbol{x}_A) = \text{Function of } [f_{\alpha,\text{interior}}, \rho_{\text{interior}}, \boldsymbol{u}_{\text{inlet}}]. \quad (50)$$

In Eq. (45), the equilibrium part of distribution function is determined by the values of known density and velocity at the inlet,

$$f_{\bar{\alpha}}^{(\mathrm{eq})}(\boldsymbol{x}_A) = \text{Function of } [\rho_{\text{inlet}}, \boldsymbol{u}_{\text{intlet}}] \quad (51)$$

which does not interact with the interior variables. In general, the $f_{\bar{\alpha}}^{(1)}$ is determined from

$$f_{\bar{\alpha}}^{(1)}(\boldsymbol{x}_A) = \text{Function of } \left[\nabla\rho_{\text{interior}}, \nabla\boldsymbol{u}_{\text{interior}}\right]. \quad (52)$$

Only when the inlet velocity is uniform, Eq. (45) reduces to Eq. (44) so that the interaction disappears.

Eqs. (43) and (45) are different in one major aspect. In Eq. (43), $\tilde{f}_{\bar{\alpha}}(\boldsymbol{x}_A)$ strongly depends on ρ and f_α's at the interior lattice nodes whereas in Eq. (45), only $f_{\bar{\alpha}}^{(1)}(\boldsymbol{x}_A)$ in $f_{\bar{\alpha}}(\boldsymbol{x}_A)$ is related the values of ρ and $\boldsymbol{u}$ in the interior nodes while $|f_\alpha^{(1)}|$ is much less than $f_\alpha^{(\mathrm{eq})}$ in general. From the above analysis, an improved treatment on the inlet boundary condition is required to minimize the impact on the inlet boundary by the interior flow variables.

5.2. *Interpolation-based superposition scheme for inlet boundary*

In what follows, an improved inlet boundary treatment recently developed in Yu [116] is summarized. To construct f_α at the inlet with minimal influence from the interior, the superposition: $f = f^{(\mathrm{eq})} + f^{(\mathrm{neq})}$ with $|f^{(\mathrm{neq})}| \ll |f^{(\mathrm{eq})}|$ is first noted. If $f_{\bar{\alpha}}^{(\mathrm{eq})}$ with $\boldsymbol{e}_{\bar{\alpha}}$ pointing toward the interior of flow field is specified and not allowed to vary with the interior flow variables, then a major portion of $f_{\bar{\alpha}}$ will be specified and remain independent of the interior flow variables. Hence, only a small portion of the incoming disturbance will be reflected back to the interior flow field through $f^{(neq)}_{\bar{\alpha}}$.

Since in general the inlet can be located anywhere between the grid points, $f^{(eq)}_{\bar{\alpha}}$ and $f^{(neq)}_{\bar{\alpha}}$ in the inlet treatment need to be obtained through interpolation. For this reason, this condition is referred to as "interpolation-based superposition scheme".

To illustrate how $f^{(eq)}_{\bar{\alpha}}$ and $f^{(neq)}_{\bar{\alpha}}$ are constructed numerically, a 1-D example is shown in Fig. 31. After the streaming step, $f_{1,B}$, which includes $f^{(eq)}_{1,B}$ and $f^{(neq)}_{1,B}$, needs to be determined. At the inlet, the fluid density and velocity are known. Thus, the equilibrium distribution function $f^{(eq)}_{1,I}$ at the inlet line can be found using Eq. (44). Using the known values of $f^{(eq)}_{1,I}$ and $f^{(eq)}_{1,C}$, $f^{(eq)}_{1,B}$ can be found easily using a linear interpolation:

$$f^{(eq)}_{1,B} = f^{(eq)}_{1,I} + \frac{\Delta}{1+\Delta}\left(f^{(eq)}_{1,C} - f^{(eq)}_{1,I}\right). \tag{53}$$

Although the distribution function $f^{(eq)}_{1,C}$ in the interior of flow filed is used to obtain the inlet condition for $f^{(eq)}_{1,B}$, it has very different characteristics than that in the bounce-back scheme. In the bounce-back scheme, $f_{1,B}(t)$ is obtained using $f_{1,B}(t) = \tilde{f}_{5,B}(t-1) + 2/3\rho_B u_x$. Since $\boldsymbol{e}_5$ is in the negative x-direction, $f_{5,B}(t-1) = \tilde{f}_{5,C}(t-2)$ due to streaming. Thus, the distribution function f_5 in the interior domain has a direct impact on $f_{1,B}(t)$. Such a strong influence is mostly lacking in Eq. (53) since $f_{1,C}(t)$ primarily depends on the macroscopic variables which are sums of all f_α's (see Eqs. (6) and (7)) and the influence of $f_{5,C}(t)$ on $f_{1,B}(t)$ is averaged out by other components. In addition since the weighting factor $\Delta/(1+\Delta)$ is always less than 0.5, it further reduces the effect of $f_{5,C}$ on $f_{1,B}$ comparing with the bounce-back scheme.

To construct $f^{(neq)}_{1,B}$, the basic idea in Eq. (53) is followed. However, $f^{(neq)}_{1,I}$ is not known. Following the similar idea in Zou and He [114], the bounce-back scheme for the non-equilibrium part at the inlet is used. By setting approximately

$$f^{(neq)}_{1,I} = f^{(neq)}_{5,B} \tag{54}$$

an interpolation for $f^{(neq)}_{1,B}$ is obtained:

$$f^{(neq)}_{1,B} = f^{(neq)}_{1,I} + \frac{\Delta}{1+\Delta}\left(f^{(neq)}_{1,C} - f^{(neq)}_{1,I}\right). \tag{55}$$

Since $f^{(neq)}$ is small in magnitude, $f^{(neq)}_{1,B}$ should have a small overall influence on $f_{1,B}$. The non-equilibrium part of the distribution function given in Eq. (55) is then added to the equilibrium distribution function given by Eq. (53). In most cases, the inlet is far away from the region of main interesting so that Δ can be set to 0 ($\boldsymbol{x}_I = \boldsymbol{x}_B$) to simplify the computation and further reduce the interaction.

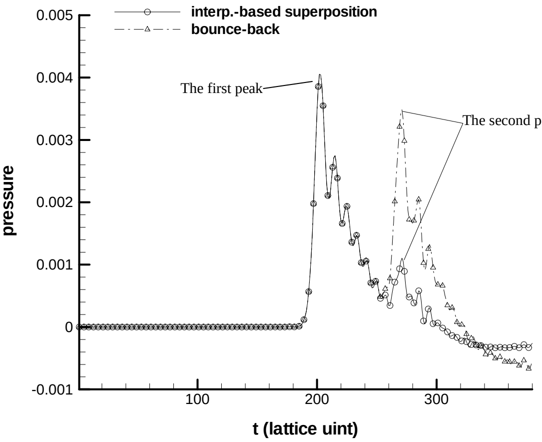

Fig. 35. Pressure variation $(\rho-1)/3$ at point M at the early stage of computation. Uniform velocity is given as initial condition [116].

This improved inlet boundary treatment was applied to a flow over a column of cylinders at $Re = 500$ [116], which was the case being used to test the bounce-back scheme at inlet in Section 5.1. In the computation, the inlet coincides with the nodes so that $\Delta = 0$. Fig. 35 compares the variation of pressure at point M by using the interpolation-base superposition scheme and the bounce-back on the link scheme. The superposition scheme produces smaller pressure fluctuation than bounce-back scheme after pressure wave has been reflected by the inlet boundary. Hence, the superposition scheme allows most of pressure oscillation to pass through the boundary almost non-reflectively while bounce-back scheme reflects most of them.

The benchmark solutions of a laminar flow over a circular cylinder asymmetrically placed inside a channel by Schäfer and Turek [103] was used to examine how the interpolation-based superposition scheme performs when inlet velocity is not uniform. In this simulation, the interpolation-based superposition scheme and bounce-back scheme were used, respectively, at the inlet. The Reynolds number based on the average inlet velocity $\bar{U}$ and cylinder diameter is 20 so that steady flow was obtained. In the computation, Δ was chosen to be 0.5 in Eqs. (53) and (55).

Both inlet conditions gave $C_D = F_x/\rho\bar{U}^2 r = 5.59$, which is within the range of 5.57–5.59 reported by Schäfer and Turek [103]. Fig. 36 shows the comparison of velocity profiles along the y-direction at first fluid node after the inlet. Fig. 37 shows shear stress profiles at the same location. It can be seen that the superposition scheme can successfully recover the velocity and stress at the inlet. In Fig. 37, shear stress profiles are already nonlinear along the y-direction because the inlet was placed not too far from the cylinder.

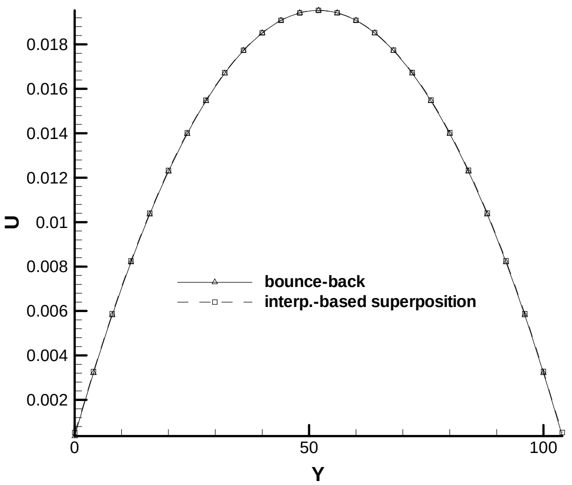

Fig. 36. Velocity profile along y-direction at nodes which are 0.5 lattice unit downstream from the inlet [116].

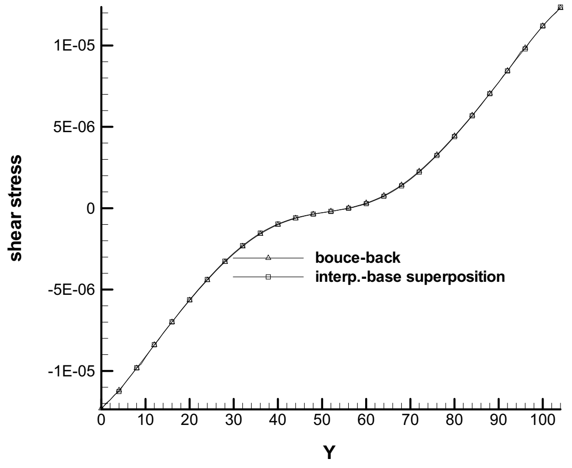

Fig. 37. Shear stress profile along y-direction at nodes which are 0.5 lattice unit downstream from the inlet [116].

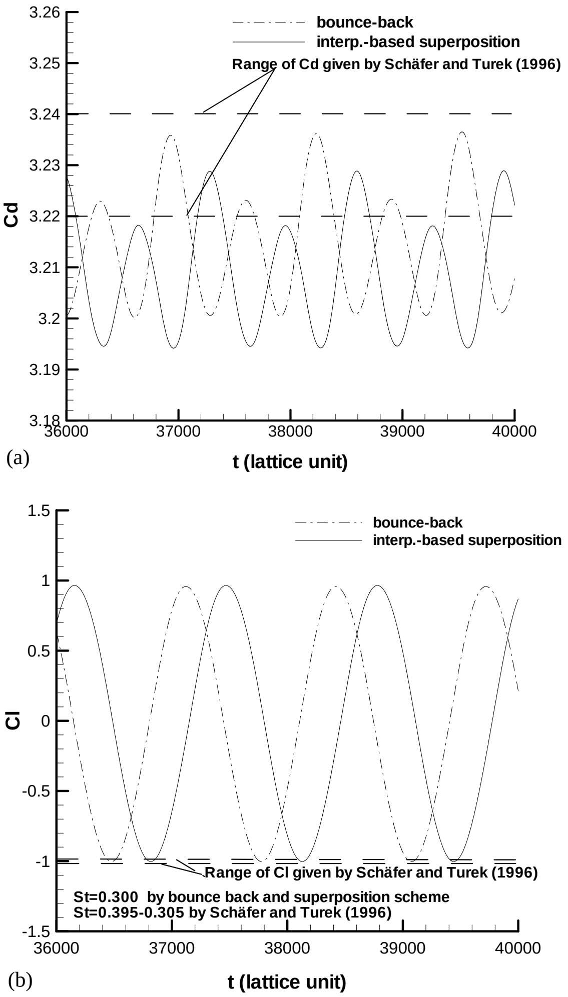

Fig. 38. Comparison of the drag coefficient (a) and lift coefficient (b) [116] with the benchmark results given in Schäfer and Turek [103].

To compare the performance of both inlet treatments in the unsteady flow case, Reynolds number was increased to 100 so that vortex shedding occurs. Figs. 38a and b compare the lift coefficient $C_{\mathrm{L}} = F_y/\rho\bar{U}^2 r$, and the drag coefficient C_{D} with the benchmark results (Schäfer and Turek, [103]). The force was evaluated using the momentum exchange method. The numerical value of Strouhal number $St = 2r/(\bar{U}T)$ is 0.300 in which T is the period of the lift curve. This agrees very well with the range of value (0.2995–0.305) given in Schäfer and Turek [103].

Using the interpolation-based superposition scheme, flows over the NACA 0012 airfoil at $Re = 500$, 1000, 2000, and 5000 were computed with the multi-block LBE method [84]. Details of these results were presented in Section 3 and in [84]. In the work of Yu et al. [84], the equilibrium distribution was used at the inlet which includes the far field boundary except at the downstream outlet. Since the open boundaries are far away from the airfoil and the velocity is nearly uniform, the superposition scheme gave the same results as the equilibrium condition.

However, the bounce-back scheme at the inlet yields unphysical transient behavior with erratic oscillations with $Re = 2000$ and 5000 ($\tau = 0.5025$ and 0.50125, respectively). Fig. 39a shows the time history of the drag coefficient with $Re = 2000$ using the bounce-back scheme while Fig. 39b shows the corresponding result using the interpolation-based superposition scheme. The latter results in fast convergence to the steady-state

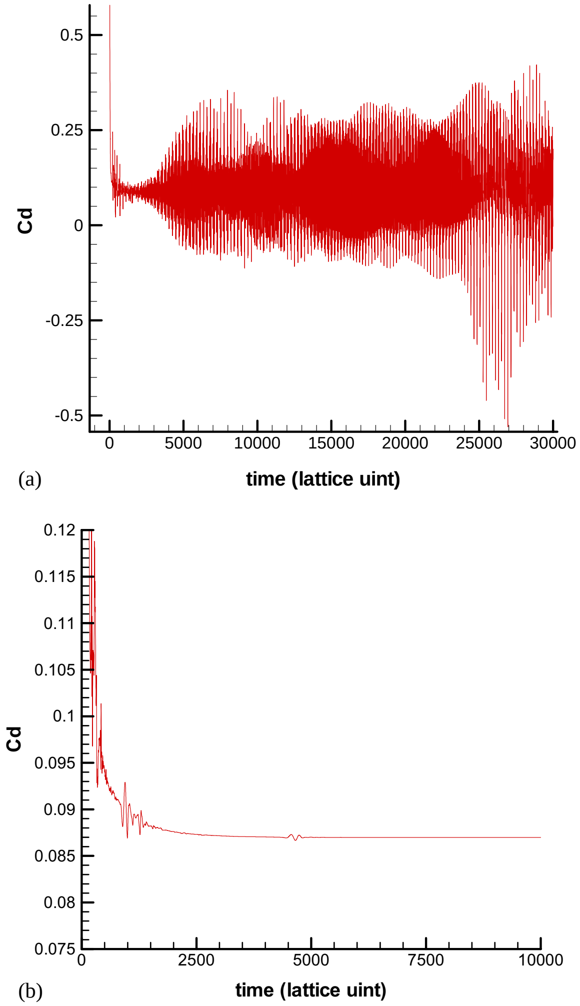

Fig. 39. (a) Drag coefficient for flow over NACA0012 airfoil at $Re = 2000$ using the bounce-back scheme for the inlet boundary [116]. (b) Convergence history of the drag coefficient for flow over NACA0012 airfoil at $Re = 2000$ using interpolation-based superposition scheme for the inlet boundary [116].

solution while the bounce-back inlet treatment is incapable of producing sensible solution at this Reynolds number.

To summarize, the standard bounce-back scheme at the inlet reflects most of pressure wave back to the interior of flow field and results in slower convergence and more pronounced fluctuation especially when the Reynolds number is high. The interpolation-based superposition scheme can reduce the impact of the boundary–interior interaction on the unsteady development of the flow field and improve the rate of convergence, the numerical stability, and the quality of the overall solution.

6. Multi-relaxation-time models

In Section 3, it is seen that the pressure field in lid-driven cavity flow can be very noisy due to the singularities at the two upper corners of flow domain. In Section 5, large pressure oscillations in flow field are observed due to the error in the initial condition. Although their effects can be reduced by employing the multi-block method and the improved inlet boundary condition, as Lallemand and Luo [93] pointed out, the solution inaccuracy is associated with the fundamental shortcoming of the SRT LBGK model. That is, it is difficult to damp out the acoustic modes in the transient pressure field at high Reynolds number when the bulk and shear viscosities have to be identical in the LBGK scheme. Problem of this nature can be easily addressed by using MRT models.

6.1. Two-dimensional multi-relaxation-time model

d'Humieres [93] presented a 2-D MRT lattice Boltzmann model for the 2-D lattice structure shown in Fig. 1. In this model, a new set of variables $\underline{R} = (\rho, e, \varepsilon, j_x, q_x, j_y, q_y, p_{xx}, q_{xy})^{\mathrm{T}}$ is introduced and $\underline{R}$ is related to the set of $\underline{F} = (f_0, f_1, f_2, f_3, f_4, f_5, f_6, f_7, f_8)^{\mathrm{T}}$ as follows:

$$\underline{R} = \begin{pmatrix} \rho \\ e \\ \varepsilon \\ j_x \\ q_x \\ j_y \\ q_y \\ p_{xx} \\ q_{xy} \end{pmatrix}$$
$$= \begin{pmatrix} 1 & 1 & 1 & 1 & 1 & 1 & 1 & 1 & 1 \\ -4 & -1 & 2 & -1 & 2 & -1 & 2 & -1 & 2 \\ 4 & -2 & 1 & -2 & 1 & -2 & 1 & -2 & 1 \\ 0 & 1 & 1 & 0 & -1 & -1 & -1 & 0 & 1 \\ 0 & -2 & 1 & 0 & -1 & 2 & -1 & 0 & 1 \\ 0 & 0 & 1 & 1 & 1 & 0 & -1 & -1 & -1 \\ 0 & 0 & 1 & -2 & 1 & 0 & -1 & 2 & -1 \\ 0 & 1 & 0 & -1 & 0 & 1 & 0 & -1 & 0 \\ 0 & 0 & 1 & 0 & -1 & 0 & 1 & 0 & -1 \end{pmatrix} \begin{pmatrix} f_0 \\ f_1 \\ f_2 \\ f_3 \\ f_4 \\ f_5 \\ f_6 \\ f_7 \\ f_8 \end{pmatrix}$$
$$= \underline{M}\,\underline{F}, \qquad (56)$$

where $\underline{M}$ is the 9×9 matrix transforming $\underline{F}$ to $\underline{R}$. In the vector $\underline{R}$, ρ is the fluid material density, e is the energy, ε is related to the square of the energy, j_x and j_y are the momentum density (or mass flux), q_x and q_y correspond to the energy flux, and p_{xx} and p_{xy} correspond to the diagonal and off-diagonal components of the viscous stress tensor. An inherent disadvantage of the SRT

LBGK model is that all variables are relaxed in the same manner as given by Eq. (10a). In lieu of Eq. (10a), the collision procedure of the MRT model is carried out as follows:

$$\tilde{e} = e - s_2(e - e^{\text{eq}}), \tag{57a}$$

$$\tilde{\varepsilon} = \varepsilon - s_3(\varepsilon - \varepsilon^{\text{eq}}), \tag{57b}$$

$$\tilde{q}_x = q_x - s_5(q_x - q_x^{\text{eq}}), \tag{57c}$$

$$\tilde{q}_y = q_y - s_4(q_y - q_y^{\text{eq}}), \tag{57d}$$

$$\tilde{p}_{xx} = p_{xx} - s_8(p_{xx} - p_{xx}^{\text{eq}}), \tag{57e}$$

$$\tilde{p}_{xy} = p_{xy} - s_9(p_{xy} - p_{xy}^{\text{eq}}), \tag{57f}$$

where $\sim$ denotes the post-collision state and s_i is the inverse relaxation time for various modes. The equilibrium values are chosen to be

$$e^{\text{eq}} = -2\rho + 3(u^2 + v^2), \tag{58a}$$

$$\varepsilon^{\text{eq}} = \rho - 3(u^2 + v^2), \tag{58b}$$

$$q_x^{\text{eq}} = -u, \tag{58c}$$

$$q_y^{\text{eq}} = -v, \tag{58d}$$

$$p_{xx}^{\text{eq}} = u^2 - v^2, \tag{58e}$$

$$p_{xy}^{\text{eq}} = uv. \tag{58f}$$

Before the streaming step, Eq. (10b), is carried out, one needs to transform the post-collision values, $\tilde{\underset{\sim}{R}}$, back to $\tilde{\underset{\sim}{f}}$ by using

$$\tilde{\underset{\sim}{f}} = \underset{\sim}{M}^{-1}\tilde{\underset{\sim}{R}}. \tag{59}$$

In practice, Eq. (59) can be combined with Eq. (57) to obtain a single expression

$$\tilde{\underset{\sim}{f}} = \underset{\sim}{F} - \underset{\sim}{M}^{-1}\underset{\sim}{S}(\underset{\sim}{R} - \tilde{\underset{\sim}{R}}), \tag{60}$$

where $\underset{\sim}{S}$ is the diagonal matrix:

$$\underset{\sim}{S} = \text{diag}(0, s_2, s_3, 0, s_5, 0, s_7, s_8, s_9). \tag{61}$$

The streaming step in the MRT model is carried out in the same manner for each component as in the SRT LBGK model based on Eq. (10b).

In Lallemand and Luo [93], it was shown that for the MRT model to give the same shear viscosity as given by Eq. (15) for the SRT model, one can set

$$s_8 = s_9 = 1/\tau. \tag{62}$$

It is more flexible to choose the rest of the relaxation parameters: s_2, s_3, s_5, and s_7. In general, these four parameters can be chosen to be slightly larger than 1. It is worth commenting here that by setting $s_2 = s_3 = s_5 = s_7 = s_8 = s_9 = 1/\tau$, the SRT LBGK model for incompressible flow [119] is recovered.

In attempting to obtain solutions for high Reynolds number flows using the LBE method, the solution field for (p, u, v) can exhibit spatial oscillations in regions of large gradients such as stagnation point and sharp convex corners [95]. Especially near a sharp convex corner, because the pressure and velocity are singular locally, large gradients in the density or pressure field exist. When there is insufficient resolution near the corner, the large gradient results in spatial oscillations. Depending on the geometry, such spatial oscillation can propagate further into the flow field to contaminate a large region of interest. The spatial oscillations often adversely affect the numerical stability and convergence rate.

Lallemand and Luo [93] performed detailed analyses on the dispersion, dissipation, and stability characteristics of the MRT lattice Boltzmann equation model. It was found that multiple relaxation times leads to better computational stability due to the separation of the relaxations of the various kinetic modes in the LBE model. It was also found in Lallemand and Luo [93] through the linearized analysis on the MRT model for various simple flows that the MRT model gives the same results, to the second-order accuracy, as the SRT LBGK model does. It seems that these two models perform similarly in the long wavelength limit for macroscopic variables of interest.

However, for fluid flows with high gradients, i.e., substantial short wavelength components, it is expected that the results of the MRT model behave noticeably differently from that of the SRT model. It is insightful to investigate how the solution based on the MRT model behaves in such flows in comparison with the SRT LBGK model.

6.2. *Comparison of performances of MRT and SRT models*

Mei et al. [95] compared the performance of the SRT and MRT models for some flows with singularity which include: (1) Stokes first problem, and (2) steady uniform flow over a cascade of zero-thickness, finite length flat plates. The flow in the Stokes first problem is singular at $t = 0$. The exact solution for the wall shear stress for Stokes first problem is given by

$$\tau_{xy,\text{w}} = -\frac{\mu U}{\sqrt{\pi v t}}, \tag{63}$$

where v is the dynamic viscosity of the fluid. Fig. 40 shows the relative error of the LBE solutions for the wall shear stress,

$$E = \frac{\left|\tau_{xy,\text{w}}^{\text{LBE}} - \tau_{xy,\text{w}}^{\text{exact}}\right|}{\left|\tau_{xy,\text{w}}^{\text{excat}}\right|}. \tag{64}$$

Near $t = 0$, there is insufficient spatial resolution for the Stokes layer of the thickness $\sqrt{vt}$. Hence, as illustrated in Fig. 40 substantial oscillations are present near $t = 0$. Clearly, the error in the MRT model is smaller than that of the SRT model for $t < 100$ when the near-wall velocity gradient is large. Eventually, the effect of singularity diminishes and the two solutions approach each other.

The flow over a flat plate has a singularity in pressure and stresses at the leading edge of the plate. A schematic of the flow is shown in the insert of Fig. 41. Reynolds number based on the length is $Re = UL/\nu = 1000$. Fig. 41 compares the density deviation, $\rho - 1$, from the far field value ($\rho = 1$) as a function of y at $x/L = 0.0125$, which is half grid away from the leading edge, based on the MRT and SRT models under otherwise identical conditions. When there is insufficient numerical resolution for high Reynolds number flows, a non-physical spatial oscillation develops near the leading edge. However, the MRT model is seen to be more effective in suppressing the spatial oscillation for ρ or p near the leading edge. Fig. 42 compares $\rho - 1$ as a function of y at $x/L = 0.5125$ under the same condition. The solution based on the SRT model still possesses a substantial level of spatial oscillations even far away from the leading edge while the solution from the MRT model has become sufficiently smooth. Fig. 43 shows the viscous normal stress, τ_{xx}, normalized by $\mu U/L$, as a function of y at $x/L = 0.5125$. Similar level of oscillations is observed in the SRT based solution.

To further develop, a quantitative understanding of the performance of the two models for flow over a flat plate, the streamwise variation of various macroscopic quantities near the plate $y/L = 0.0125$, which is half-grid

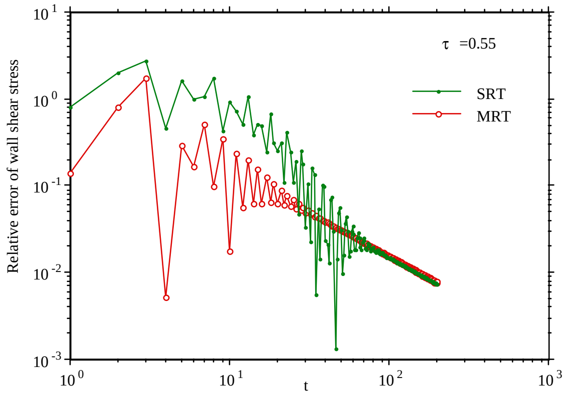

Fig. 40. Comparison of the relative error in the evolution of the wall shear stress for Stokes first problem between the SRT and MRT models [95].

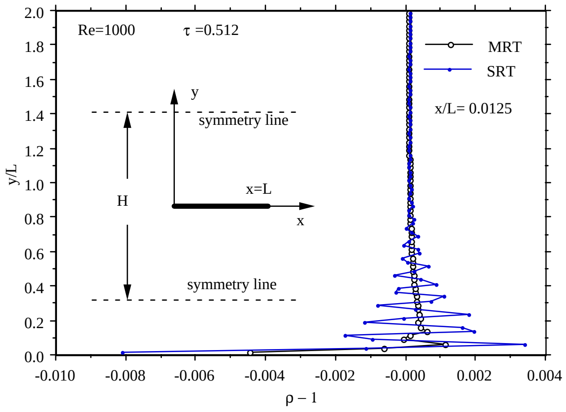

Fig. 41. Comparison of the density profiles near the leading edge ($x/L = 0.0125$) between the SRT model and MRT model at $Re = 1000$ [95].

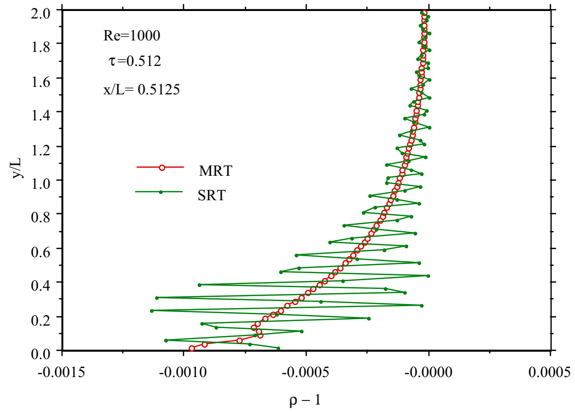

Fig. 42. Comparison of the density profiles at $x/L = 0.5125$ between the SRT model and MRT model at $Re = 1000$ [95].

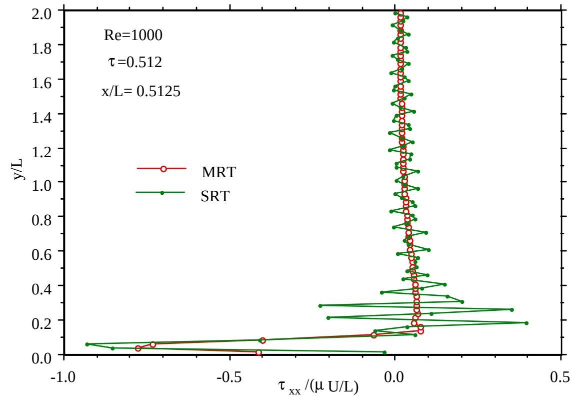

Fig. 43. Comparison of the viscous normal stress profiles at $x/L = 0.5125$ between the SRT model and MRT model at $Re = 1000$ [95].

above the plate, were also examined. Fig. 44 shows the variation of the pressure coefficient

$$C_p = \frac{p - p_\infty}{\rho_0 U^2/2}, \tag{65}$$

at $y/L = 0.0125$ as a function of x for solutions based on these two models where p_∞ is the pressure at the centerline of the inlet. It is noted that the singularity at $x = 0$ resulted in oscillation in C_p for about 4–5 grid points after the leading edge in the MRT model.

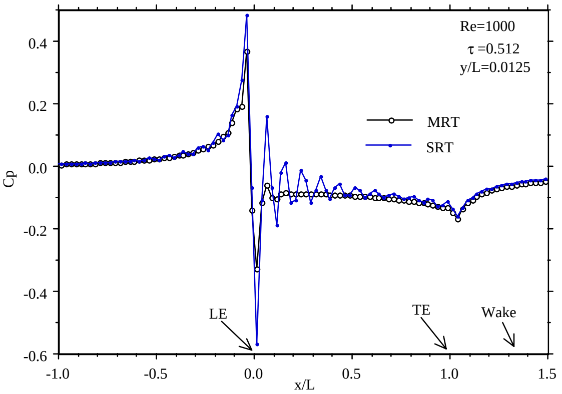

Fig. 44. Comparison of pressure coefficient as a function of x at $y/L = 0.0125$ between the SRT model and MRT model [95].

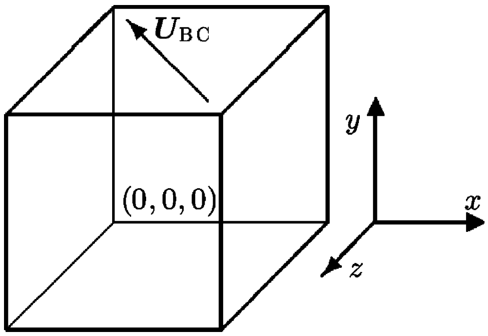

Fig. 45. Diagonally driven cavity flow.

However, C_p in the SRT-based solution continues to oscillate across the entire plate.

d'Humières et al. [120] proposed a 3-D MRT model and compared its performance with SRT LBGK D3Q15 model in simulating Povitsky cavity flow, as illustrated in Fig. 45. Fig. 46 shows the pressure contours at $z = 0.5$ at $Re = 500$. It can be seen that large pressure oscillation exists in the region even far from the singularity points by using the SRT model, in contrast to the much smoother pressure field obtained by using the MRT model. At $Re = 2000$, the SRT model cannot yield steady-state solution, while the MRT model can obtain satisfactory results.

Due to the ability to independently adjust the bulk viscosity, the MRT model has substantial advantages over the SRT model in handling the geometric singularities. The MRT model in general can produce smoother variations of the macroscopic quantities with much smaller regions of oscillations near a singularity. Since the spatial oscillation is also often accompanied by the pressure waves in transient simulations, the MRT model also offers a better convergence toward steady state.

7. Recent developments and applications of the LBE method

7.1. Thermal and compressible LBE schemes

There has been an ongoing effort in construction of stable LBE models and schemes to simulate fully compressible and thermal flows [121–142]. The existing thermal lattice Boltzmann equation (TLBE) models can be classified into three categories. The first category, which is also the simplest approach, is that of passive scalar [121,122,123]. In this approach, the temperature is treated as a passive scalar which is advected by the flow velocity but does not affect the flow fields (density and velocity). The flow fields and the passive-scalar temperature are represented by two sets of distribution functions: one simulates the NS equation, and the other simulates the advection-diffusion equation satisfied by

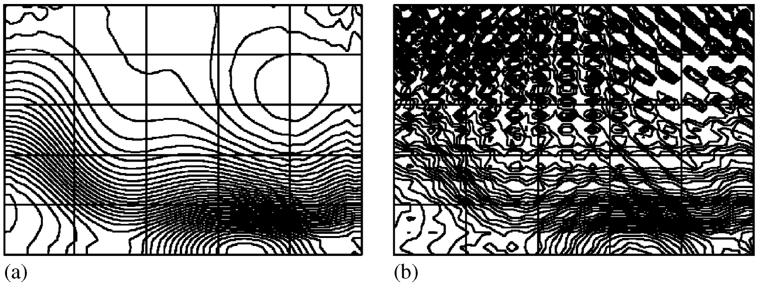
(a) (b)

Fig. 46. Cavity flow $Re = 500$ computed by d'Humières et al. [120], pressure contours at $z = 0.5$: (a) MRT and (b) LBGK.

the passive scalar driven by the flow [121,122]. Numerically, this is not very efficient because there is no need to use a full set of distribution functions to simulate a passive scalar, even though this numerical inefficiency can be improved somewhat by using some redundant degree of freedom in some LBE models [123]. The limitation of this approach is obvious and therefore this is not a viable approach.

The second category of the TLBE models includes various shock capturing schemes based on the LBE method to treat fully compressible Euler [124–126] or NS [127–130] equations. It should be noted that the equilibrium distribution functions in all LBE Euler schemes are polynomials of hydrodynamic variables: density, velocity, and internal energy (or temperature), and therefore the Mach number cannot be too large. In LBE NS schemes, in order to allow large speeds, the advection step is adapted to the local flow velocity [143] thus it is no longer a simple process of hopping from one grid point to the next—interpolations must be employed in some way. The equilibrium distribution function can be a polynomial [127] or other more complicated algebraic functions [128], or a Kronecker Delta function which helps to increase the Mach number [129]. It is important to note that the numerical analysis for the LBE shock capturing schemes is yet to be done—the numerical accuracy of these schemes remains by and large unknown. Thus, the LBE shock capturing schemes are in a premature stage.

The third category of the TLBE models is straightforward modifications of their athermal counterparts. The TLBE models in this third category incorporate energy conservation law, and are characterized by low Mach number and Boussinesq approximations. The essence of Boussinesq approximation is that the density variation only appears in the force term (the buoyancy force); all the transport coefficients (viscosities and heat conductivity) and the sound speed are considered to be independent of temperature. There has been a number of proposals to make the energy-conserving LBE capable of simulating thermohydrodynamics:

1. to increase the number of velocities [131,133], and to include higher-order nonlinear terms (in flow velocity) in the equilibrium distribution function [131];
2. to use an equilibrium distribution depending on variable temperature [124,131,132];
3. to implement an advection with finite difference schemes, such as Lax–Wendroff scheme, to improve numerical stability [135];
4. to use two sets of distribution functions for particle number density and energy density which effectively doubles the number of discrete velocities [136–138]. This is based on the fact that certain Gaussian quadratures associated with the LBE models can preserve the energy and heat flux exactly [32,33];
5. to use a velocity set with higher-order symmetry [140]. Unfortunately, this approach also uses anisotropic interpolations that drastically increase the numerical viscosities and anisotropic effects;
6. to use energy-dependent discrete velocities [141]. Again, anisotropic interpolations must be used in this case;
7. to use a hybrid scheme in which the flow simulation is decoupled from the solution of the temperature equation. Specifically, the flow simulation is accomplished by using the LBE while the temperature equation is solved by using finite difference schemes [142] or other means.

In spite of all the effort, the success of the TLBE remains rather limited. It is not yet as competitive as the athermal LBE, and it cannot perform as well as traditional CFD methods in many aspects. As it has been noticed previously, the main difficulty the TLBE faces is the numerical instability. Although there are some discussions of the numerical instability in the TLBE schemes [30,133,140], so far the nature of the numerical instability is not well understood until very recently.

The recent work of Lallemand et al. [144–146] pointed out that the origin of the TLBE (energy-conserving) models is due to the algebraic coupling of the viscous mode and the energy mode of the linearized system. This coupling occurs in a wide range of the wave-number k along certain directions, hence the TLBE models are prone to numerical instabilities which can be instigated by fluctuations in a broad range of scales. In contrast, for the athermal LBE models the similar coupling only occurs when the wave-number k is near π (i.e. close to the size of two grid spacings), making the athermal LBE models only sensitive to the small scale fluctuations—the athermal LBE models can be extremely stable if small scale fluctuations are dealt with care [93]. It is also observed that the algebraic coupling between the modes cannot be easily removed by increasing the number of discrete velocities. It is intrinsic to the simplicity of the spatial-temporal evolution of and the linearity of the collision operator in the energy-conserving LBE.

To overcome this difficulty, a hybrid thermal LBE method is proposed in which the mass and momentum conservation laws are solved by the usual athermal LBE, while the advection-diffusion equation satisfied by the temperature is solved separately by finite difference technique (or by other means). In this approach the energy conservation law is completely divorced from the mass and momentum conservation laws, and therefore the spurious coupling between the modes is removed. In addition to the improvement of numerical stability, the proposed hybrid TLBE method is numerically efficient. It uses fewer degrees of freedom when compared to the energy-conserving TLBE methods. The hybrid TLBE scheme has been successfully applied to simulate thermal convective flow in a cubic cavity [146]. Two noteworthy features of the hybrid TLBE method deserve to be pointed out. First of all, besides the improvement of the numerical stability, Prandtl number is adjustable when the MRT models are used, while the Prandtl number is fixed to unity for the BGK models. And second, the hybrid TLBE model does not use Boussinesq approximation explicitly. It can be extend to situations where Boussinesq approximation does not apply by using temperature dependent transport coefficients [144–146].

7.2. Multi-phase and multi-component LBE models

Simulations of multi-phase and multi-component flows are among the most successful applications of the LBE. (By multi-phase and multi-component fluids we mean the fluids with phase changes, e.g., non-ideal gases, and fluids consisting of species with different molecular properties, e.g., binary mixtures, respectively.) Although there are a lot of successful applications, most LBE models for multi-phase and multi-component fluids are based on heuristic ideas and have connections to the corresponding lattice-gas automata models. These models work well in practice. However, only recently it is shown that the LBE model for multi-phase fluids can be rigorously derived from the Enskog equation [147,148]—a counterpart of the Boltzmann equation for non-ideal gases. And the LBE model for multi-component fluids can also be rigorously derived from the corresponding kinetic equations [149,150]. These recent theoretical results [147–150] have provided a unified framework to treat the LBE models for multi-phase and multi-component fluids and thus set these models on a more rigorous foundation.

There are several areas in which the multi-phase and multi-component LBE methods have demonstrated its computational advantages. One such area is the simulation of complex fluids including colloidal suspensions [52–54], bubbles [151,152], solid particle suspension [59–70], and polymer-solvent systems [153–155]. The reason that the LBE method is effective in dealing with the suspension flow is that the method can accurately capture the hydrodynamic interactions in these systems without prohibitive computational cost.

A second area in which the LBE method has made a noticeable impact is simulations of interfacial dynamics among different fluids. The LBE method has been successfully applied to simulate droplet interactions [156,157], droplet deformation and breakup [158–160] and spreading [161,162], free-surface phenomena [163], and the Rayleigh–Taylor instability [164–166]. The LBE method shows its computational advantages when applied to the multi-phase and multi-component flow situations with complicated boundaries such as porous media [167–175]. There is a sufficient amount of evidence to demonstrate the viability and competitiveness of the LBE method for interfacial dynamics.

7.3. LBE simulations of particulate suspensions

Because the lattice Boltzmann method has been demonstrated as an effective simulation tool for particulate suspensions in fluids [52–70] that are ubiquitous in many industries, such as printing and paper-making, petroleum, bioengineering, pharmaceuticals and food processing, we shall concisely review the work in this area. The treatment of the particle–fluid interface is the central issue in the LBE simulations for suspensions in fluids. The lattice Boltzmann method uses a uniform Cartesian mesh for such simulations, and the solid–fluid interfaces are usually handled by using the bounce-back scheme [176] combined with interpolations [88,89,96, 177–179]. This treatment for moving boundaries seems to work well for LBE simulations of particulate suspensions. In contrast to many traditional methods, the lattice Boltzmann method appears to have computational advantages in simulating systems of suspending particles with sharp edges [59–62].

The LBE method has been successfully applied to simulate suspensions with single [60,64,65,67,70] or multiple particles [53,56,59–63]. The LBE simulations of a single particulate suspension in fluid have been able to accurately reproduce many results observed in experiments [59,60,66,67] and, more interestingly, to yield new results yet to be observed in experiments [64,65]. The lattice Boltzmann simulations for the suspensions of multiple particles [53,56,59–63], chains of particles [153–155], and colloidal suspensions [52–54,57,58] have also yield interesting results. It is important to point out that although the lattice Boltzmann method has been very effective and efficient in computing the overall properties of these complex fluids, the method is still not sufficiently mature for other applications such as high-Mach-number and/or high-Reynolds-number aerodynamic flows because it has not been developed for those purposes [107].

7.4. LBE simulations of turbulent flows

The LBE has been successfully tested for various laminar flows such as channel with expansions [180], cavity flows [76,120], flows past a circular cylinder [78,79] and a square cylinder [180] and flow over airfoil [84,181]. It can be rigorously shown that the LBE method is in fact a multi-dimensional finite difference scheme with the accuracy of first order in time and second order in space [182–184]. The LBE method has also been used to simulate turbulent flows in two [185, 186] and three dimensions [187–190]. A recent benchmark study comparing the pseudo-spectral and the LBE simulations of the 3-D homogeneous isotropic turbulence in a periodic box shows that the LBE method is indeed accurate and particularly suitable for Beowulf-type cluster computers [190].

More recently, the LBE method has also been used to perform large-eddy simulations (LES) [191–198] with the Smagorinsky eddy viscosity model [199]. A recent study [196, 198] of the flow past a surface mounted cube in fully developed channel flow [200, 201] provides a significant validation for the LBE-LES approach. It must be emphasized that most studies of LBE-LES methodology remain preliminary at this stage and much research is yet to be done.

7.5. LBE simulations of micro-flows

In contrast to macro flows described by continuum mechanics, micro-flows are dominated by the following four effects: (1) non-continuum effects; (2) surface-dominated effects; (3) low Reynolds number effects; and (4) multi-scale and multi-physics effects [202]. Kinetic theory (i.e. the Boltzmann equation) is capable of dealing with these effects to certain extent [202]. Due to its kinetic origin, the LBE method has the potential to simulate micro-flows for which the continuum description is invalid. However, no theoretical work has been done in this direction so far. Only very recently, the LBE method has been successfully applied to micro-flows [203–206] including the pressure-driven microchannel flow [204], mixing of binary fluids in microchannels with patterned substrates and fluid-substrate interaction [203,206], and electrokinetic flow around a corner or a wedge in microchannels [205]. These results are only preliminary, and yet to be analyzed theoretically and verified experimentally. However, these preliminary results are encouraging, and they do indicate the possibility of applying the LBE method for micro-flows.

8. Concluding remarks

In this review, critical issues in the LBE simulation for fluid flows, especially for high Reynolds number flows, are addressed. The multi-block method can greatly improve the numerical efficiency. To further improve the computational efficiency and the flexibility of the method, the adaptive mesh refinement [207] is more desirable. The adaptive mesh refinement method has been successfully applied in solving Euler and NS equation using Cartesian grid or unstructured grid [208,209]. Based on the authors' experience in developing the multi-block LBE method, it is anticipated that the successful application of adaptive mesh refinement in the LBE method will require careful treatments at the block interface in order to reduce the numerical inaccuracy.

Second-order accurate boundary conditions have been developed for curved solid body moving with a given velocity. However, when boundary moves and crosses the nodes, there is a continuous conversion between solid nodes and their neighboring fluid nodes and the total number of the boundary nodes is not fixed. This poses a challenge to the accurate evaluation of the fluid dynamic force on the body. Furthermore, it brings in extra computational noise near the body. This issue has not been adequately addressed at high Reynolds number.

Multi-relaxation-time models have been demonstrated to be beneficial in many respects for single-phase flows. It is strongly desirable to extend the MRT model to multi-component flows.

For high Reynolds number flows, while direct numerical simulation and large eddy simulation using LBE method have been carried out [191,197], engineering turbulence models in the context of the LBE method are lacking and more research efforts are required.

Acknowledgements

The authors acknowledge the support for this research from the NASA Langley Research Center under the program of Innovative Algorithms for Aerospace Engineering Analysis and Optimization, as well as from University Reesearch, Education and Technology Institute (URETI) program. LSL would also like to acknowledge the support of the United States Air Force Office for Scientific Research under Grant No. F49620-01-1-0142.

References

[1] Alves AS, editor. Discrete models of fluid dynamics, Figueira da Foz, Portugal, September 19–22, 1990. Singapore: World Scientific, 1991.

[2] Verheggen TMM, editor. Numerical methods for the simulation of multi-phase and complex flow. Proceedings of a Workshop held at Koninklijke/Shell-Laboratorium, Amsterdam, The Netherlands, May 30–June 1, 1990. Berlin: Springer, 1992.

[3] Lebowitz JL, Orszag SA, Qian YH, editors. Proceedings of the Fifth International Conference on Discrete Models for Fluid Mechanics. Princeton, NJ, June 27–29, 1994. J Stat Phys 1995;81(1/2):1–538.

[4] Boghosian BM, Alexander FJ, Coveney PV, editors. Proceedings of the 1996 Conference on Discrete Models for Fluid Mechanics, Boston, MA, August 26–28, 1996. Int J Mod Phys C 1997;8(4):637–1011.

[5] Boghosian BM, editor. Proceedings of the Seventh International Conference on the Discrete Simulation of Fluids, Oxford, UK, July 14–18, 1998. Int J Mod Phys C 1998;9(8):1123–617.

[6] Ohashi H, Chen Y, editors. Proceedings of the Eighth International Symposium on the Discrete Simulation of Fluid Dynamics, Tokyo, Japan, July 28–30, 1999. Comp Phys Commun 2000;129(1–3):1–291.

[7] Lebowitz JL, editor. Special Issue Based on the Ninth Annual International Conference on Discrete Simulation of Fluid Dynamics, Santa Fe, NM, August 21–24, 2000. J Stat Phys 2002;107(1/2):1–598.

[8] Coveney PV, Succi S, editors. Discrete modelling and simulation of fluid dynamics, the 10th International Conference on Discrete Simulation of Fluid Dynamics, Cargese, July 2–6, 2001. Philos Trans R Soc London A 2002;360(1792):1–573.

[9] Monaco R, Preziosi L. Fluid dynamic applications of the discrete Boltzmann equation. Singapore: World Scientific; 1991.

[10] Chopard B, Droz M. Cellular automata modeling of physical systems. Cambridge, UK: Cambridge University Press, 1998.

[11] Wolf-Gladrow DA. Lattice-gas cellular automata and lattice Boltzmann models. Berlin: Springer, 2000.

[12] Succi S. The lattice Boltzmann equation for fluid dynamics and beyond. New York: Oxford University Press, 2001.

[13] Benzi R, Succi S, Vergassola M. The lattice Boltzmann equation theory and applications. Phys Rep 1992;222: 45–197.

[14] Qian YH, Succi S, Orszag SA. Recent advances in lattice Boltzmann computing. In: Stauffer D, editor. Annual reviews of computational physics III. Singapore: World Scientific, 1996.

[15] Chen S, Doolen GD. Lattice Boltzmann method for fluid flows. Ann Rev Fluid Mech 1998;30:329–64.

[16] Luo L-S, Future of LGA. LBE methods. In: Salas MA, Anderson WK, editors. Computational aerosciences in the 21st century. Dordrecht: Kluwer, 2000. p. 165–87. (Available at http://www.icase.edu/~luo/publications.html).

[17] Luo L-S. The lattice-gas and lattice Boltzmann methods: past, present, and future. In: Wu J-H, Zhu Z-J, editors. Proceedings of the International Conference on Applied Computational Fluid Dynamics, Beijing, China, 2000. p. 52–83.

[18] Hardy J, de Pazzis O, Pomeau Y. Molecular dynamics of a classical lattice gas: transport properties and time correlation functions. Phys Rev A 1976;13:1949–61.

[19] Frisch U, Hasslacher B, Pomeau Y. Lattice-gas automata for the Navier–Stokes equations. Phys Rev Lett 1986;56: 1505–8.

[20] Frisch U, d'Humieres D, Hasslacher B, Lallemand P, Pomeau Y, Rivet J-P. Lattice gas hydrodynamics in two and three dimensions. Complex System 1987;1:649–707.

[21] Wolfram S. Cellular automata and complexity: collected papers. New York: Addison-Wesley, 1994.

[22] Rivet J-P, Boon JP. Lattice Gas Hydrodynamics. Cambridge, UK: Cambridge University Press, 2001.

[23] Peyret R, Taylor TD. Computational technique for fluid dynamics, vol. II. New York: Springer, 1983.

[24] Fletcher CAJ. Computational techniques for fluid dynamics, vols. I and II. New York: Springer, 1988.

[25] McNamara G, Zanetti G. Use of the Boltzmann equation to simulate lattice-gas automata. Phys Rev Lett 1988;61:2332–5.

[26] Higuera FJ, Jiménez J. Boltzmann approach to lattice gas simulations. Europhys Lett 1989;9:663–8.

[27] Koelman JMVA. A simple lattice Boltzmann scheme for Navier–Stokes fluid flow. Europhys Lett 1991;15: 603–7.

[28] Qian YH, d'Humières D, Lallemand P. Lattice BGK models for Navier Stokes equation. Europhys Lett 1992;17:479–84.

[29] Chen H, Chen S, Matthaeus WH. Recovery of the Navier–Stokes equations using a lattice-gas Boltzmann method. Phys Rev A 1992;45:R5339–42.

[30] d'Humières D. Generalized lattice Boltzmann equations. In: Shizgal D, Weaver DP, editors. Rarefied Gas Dynamics: theory and simulations. Prog Astronaut Aeronaut 1992;159:450–8.

[31] Bhatnagar PL, Gross EP, Krook M. A model for collision processes in gases, I. small amplitude processes in charged and neutral one-component system. Phys Rev 1954;94:511–25.

[32] He X, Luo L-S. A priori derivation of the lattice Boltzmann equation. Phys Rev E 1997;55:R6333–6.

[33] He X, Luo L-S. Theory of the lattice Boltzmann equation: from Boltzmann equation to lattice Boltzmann equation. Phys Rev E 1997;56:6811–7.

[34] Broadwell JE. Study of rarefied shear flow by the discrete velocity method. J Fluid Mech 1964;19:401–4.

[35] Broadwell JE. Shock structure in a simple discrete velocity gas. Phys Fluids 1964;7:1243–7.

[36] Gatignol R. Théorie Cinétique des Gaz à Répartition Discrète des Vitesses. Lecture Notes in Physics, vol. 36. Berlin: Springer, 1975.

[37] Goldstein D, Sturtevant B, Broadwell JE. Investigations of the motion of discrete-velocity gases. In: Muntz R, Weaver DP, Campbell DH, editors. Rarefied gas dynamics: theoretical and computational techniques. Prog Astronaut Aeronaut 1989;118:100–117.

[38] Inamuro T, Sturtevant B. Numerical study of discrete-velocity gases. Phys Fluids A 1990;2:2196–203.

[39] Bobylev AV. Relationships between discrete and continuous kinetic theories. In: Brun R, Campargue R, Gatignol R, Lengrand JC, editors. Rarefied Gas Dynamics: Proceedings of the 21st International Symposium on Rarefied Gas Dynamics, Marseille, France, July 26–31, 1998. Toulouse: CEPAD, 1999. p. 19–30.

[40] Mieussens L. Discrete velocity model and implicit scheme for the BGK equation of rarefied gas dynamics. Math Models Methods Appl Sci 2000;10:1121–49.

[41] Mieussens L. Discrete-velocity models and numerical schemes for the Boltzmann–BGK equation in plane and axisymmetric geometries. J Comput Phys 2000;162: 429–66.

[42] Mieussens L. Convergence of a discrete-velocity model for the Boltzmann–BGK equation. Comp Math Appl 2001;41:83–96.

[43] Luo L-S. Some recent results on discrete velocity models and ramifications for lattice Boltzmann equation. Comp Phys Commun 2000;129:63–74.

[44] Cao N, Chen S, Jin S, Martinez D. Physical symmetry and lattice symmetry in lattice Boltzmann method. Phys Rev E 1997;55:R21–4.

[45] Mei R, Shyy W. On the finite difference-based lattice Boltzmann method in curvilinear coordinates. J Comput Phys 1998;143:426–48.

[46] Tölke J, Krafczyk M, Schulz M, Rank E. Implicit discretization and nonuniform mesh refinement approaches for FD discretization of LBGK models. Int J Mod Phys C 1998;9(8):1143–57.

[47] Kandhai D, Soll W, Chen S, Hoekstra A, Sloot P. Finite-difference lattice-BGK methods on nested grids. Comput Phys Commun 2000;129:100–9.

[48] Chapman S, Cowling TG. The mathematical theory of nonuniform gases. Cambridge: Cambridge University Press; 1970.

[49] Strumolo G, Viswanathan B. New directions in computational aerodynamics. Phys World 1997;10:45–9.

[50] He X, Zhang R, Chen S, Doolen G. On the three-dimensional Rayleigh–Taylor instability. Phys Fluids 1999;11:1143–52.

[51] Martys NS, Chen H. Simulation of multicomponent fluids in complex three-dimensional geometries by the lattice Boltzmann method. Phys Rev E 1996;53:743–50.

[52] Ladd AJC. Numerical simulation of particular suspensions via a discretized Boltzmann equation. Part 1. Theoretical foundation. J Fluid Mech 1994;271:285–309.

[53] Ladd AJC. Numerical simulation of particular suspensions via a discretized Boltzmann equation. Part 2. Numerical results. J Fluid Mech 1994;271:311–39.

[54] Ladd AJC, Verberg R. Lattice Boltzmann simulations of particle fluid suspensions. J Stat Phys 2001;104:1191–251.

[55] Nguyen N-Q, Ladd AJC. Lubrication corrections for lattice Boltzmann simulations of particle suspensions. Phys Rev E 2002;66:046708.

[56] Ladd AJC. Effects of container walls on the velocity fluctuations of sedimenting spheres. Phys Rev Lett 2002;88:048301.

[57] Heemels MN, Hagen MHJ, Lowe CP. Simulating solid colloidal particles using the lattice-Boltzmann method. J Comput Phys 2000;164:48–61.

[58] Horbach J, Frenkel D. Lattice-Boltzmann method for the simulation of transport phenomena in charged colloids. Phys Rev E 2001;64:061507.

[59] Qi D. Non-spherical colloidal suspensions in three-dimensional space. Int J Mod Phys C 1997;8:985–97.

[60] Qi D. Lattice Boltzmann simulation of particles in non-zero-Reynolds-number flows. J Fluid Mech 1999;385:41–62.

[61] Qi D. Lattice-Boltzmann simulations of fluidization of rectangular particles. Int J Multiph Flow 2000;26:421–33.

[62] Qi D. Simulations of fluidization of cylindrical multiparticles in a three-dimensional space. Int J Multiph Flow 2000;27:107–18.

[63] Qi D, Luo L-S, Aravamuthan R, Strieder W. Lateral migration and orientation of elliptical particles in Poiseuille flows. J Stat Phys 2002;107:101–20.

[64] Qi D, Luo L-S. Rotational and orientational behaviour of a three-dimensional spheroidal particles in Couette flow. J Fluid Mech 2003;447:201–3.

[65] Qi D, Luo L-S. Transitions in rotations of a non-spherical particle in a three-dimensional moderate Reynolds number Couette flow. Phys Fluids 2002;12:4440–3.

[66] Aidun CK, Lu YN, Ding EJ. Direct analysis of particulate suspensions with inertia using the discrete Boltzmann equation. J Fluid Mech 1998;373:287–311.

[67] Ding EJ, Aidun CK. The dynamics and scaling law for particles suspended in shear flow with inertia. J Fluid Mech 2000;423:317–44.

[68] Ding EJ, Aidun CK. Extension of the lattice-Boltzmann method for direct simulation of suspended particles near contact. J Stat Phys 2002, to appear.

[69] Feng ZG, Michaelides EE. Interparticle forces and lift on a particle attached to a solid boundary in suspension flow. Phys Fluids 2002;14:49–60.

[70] Clague DS, Cornelius PJ. The hydrodynamic force and torque on a bounded sphere in Poiseuille flow. Int J Numer Methods Fluids 2002;35:55–70.

[71] Chen S, Dawson SP, Doolen GD, Janecky DR, Lawniczak A. Lattice methods and their applications to reacting systems. Comput Chem Eng 1995;19:617–46.

[72] Yu H, Luo L-S, Girimaji SS. Scalar mixing and chemical reaction simulations using lattice Boltzmann method. Int J Computat Eng Sci 2002;3:73–87.

[73] Chen S, Chen H, Martínez D, Matthaeus WH. Lattice Boltzmann model for simulation of magnetohydrodynamics. Phys Rev Lett 1991;67:3776–9.

[74] Miller W, Succi S, Mansutti D. A lattice Boltzmann model for anisotropic liquid/solid phase transition. Phys Rev Lett 2001;86:3578–81.

[75] Miller W, Succi S. A lattice Boltzmann model for anisotropic crystal growth from melt. J Stat Phys 2002;107:173–86.

[76] Hou S, Zou Q, Chen S, Doolen G, Cogley AC. Simulation of cavity flow by the lattice Boltzmann method. J Comput Phys 1995;118:329–47.

[77] Luo L-S. Symmetry breaking of flow in 2D symmetric channels: simulations by lattice-Boltzmann method. Int J Mod Phys 1997;8:859–67.

[78] He X, Doolen G. Lattice Boltzmann method on a curvilinear coordinate system: vortex shedding behind a circular cylinder. Phys Rev E 1997;56:434–40.

[79] He X, Doolen D. Lattice Boltzmann method on curvilinear coordinates systems: flow around a circular cylinder. J Comput Phys 1997;134:306–15.

[80] Amati G, Succi S, Piva R. Massively parallel lattice-Boltzmann simulation of turbulent channel flow. Int J Mod Phys C 1997;8:869–77.

[81] Amati G, Benzi R, Succi S. Extended self-similarity in boundary-layer turbulence. Phys Rev E 1997;55:6985–8.

[82] He X, Zou Q, Luo L-S, Dembo M. Some progress in the lattice Boltzmann method. Part I, non-uniform mesh grids. J Comput Phys 1996;129:357–63.

[83] Filippova O, Hänel D. Grid refinement for lattice-BGK models. J Comput Phys 1998;147:219–28.

[84] Yu D, Mei R, Shyy W. A multi-block lattice Boltzmann method for viscous fluid flows. Int J Numer Methods Fluids 2002;39:99–120.

[85] Ziegler DP. Boundary conditions for lattice Boltzmann simulations. J Stat Phys 1993;71:1171–7.

[86] Ginzbourg I, Alder PM. Boundary flow condition analysis for the three-dimensional lattice Boltzmann model. J Phys II France 1994;4:191–214.

[87] Mei R, Luo L-S, Shyy W. An accurate curved boundary treatment in the lattice Boltzmann method. J Comput Phys 1999;155:307–30.

[88] Bouzidi M, Firdaouss M, Lallemand P. Momentum transfer of a lattice Boltzmann fluid with boundaries. Phys Fluids 2001;13:3452–9.

[89] Yu D, Mei R, Shyy W. A unified boundary treatment in lattice Boltzmann method. New York: AIAA 2003-0953, 2003.

[90] Cornubert R, d'Humières D, Levermore D. A Knudsen layer theory for lattice gases. Physica D 1991;47:241–59.

[91] Behrend Q. Solid–fluid boundaries in particle suspension simulation via the lattice Boltzmann method. Phys Rev E 1995;52:1164–75.

[92] Ginzbourg I. Boundary condition problems in lattice gas methods for single and multiple phases. PhD thesis, Université Paris VI, 1994.

[93] Lallemand P, Luo L-S. Theory of the lattice Boltzmann method: dispersion, dissipation, isotropy, Galilean invariance, and stability. Phys Rev E 2000;61:6546–62.

[94] Dellar PJ. Bulk and shear viscosities in lattice Boltzmann equations. Phys Rev E 2001;64:031203.

[95] Mei R, Yu D, Shyy W. Assessment of the multi-relaxation-time and single-relaxation-time models in the lattice Boltzmann equation method. New York: AIAA paper 2001-2666, 2001.

[96] Mei R, Yu D, Shyy W, Luo L-S. Force evaluation in the lattice Boltzmann method involving curved geometry. Phys Rev E 2002;65:041203.

[97] Shyy W, Liu J, Wright J. Pressure-based viscous flow computation using multiblock overlapping curvilinear grid. Numer Heat Transfer 1994;25:39–59.

[98] Shyy W. Computational modeling for fluid flow and interfacial transport, corrected printing. Amsterdam: Elsevier, 1997.

[99] Shyy W, Thakur SS, Ouyang H, Liu J, Blosch E. Computational techniques for complex transport phenomena. New York: Cambridge University Press, 1999.

[100] Fornberg B. Steady incompressible flow past a row of circular cylinder. J Fluid Mech 1991;225:655–71.

[101] Mei R, Shyy W, Yu D, Luo L-S. Lattice Boltzmann method for 3-D flows with curved boundary. J Comput Phys 2000;161:680–99.

[102] Bouzidi M, d'Humières D, Lallemand P, Luo L-S. Lattice Boltzmann equation on a two-dimensional rectangular grid. J Comput Phys 2001;172:704–17.

[103] Schäfer M, Turek S. Benchmark computations of laminar flow around a cylinder. In: Hirshel H, editor. Flow Simulation with High-Performance Computers II. Notes on Numerical Fluid Mechanics, vol. 52. Braunschweig: Vieweg, 1996. p. 547–66.

[104] Lin CL, Lai YG. Lattice Boltzmann method on composite grids. Phys Rev E 2000;62:2219–25.

[105] Ghia U, Ghia KN, Shin CT. High-Re solution for incompressible flow using the Navier–Stokes equations and a multigrid method. J Comput Phys 1982;48:387–411.

[106] Drela M, Giles MB. Viscous-inviscid analysis of transonic and low Reynolds number airfoils. AIAA J 1987;25:1347–55.

[107] Lockard DP, Luo L-S, Milder SD, Singer BA. Evaluation of powerflow for aerodynamic applications. J Stat Phys 2002;107:423–78.

[108] Wolfram S. Cellular automaton fluids. 1: basic theory. J Stat Phys 1986;45:471–526.

[109] Lavallee P, Boon JP, Noullez A. Boundaries in lattice gas flows. Physica D 1991;47:233–40.

[110] Noble DR, Chen S, Georgiadis JG, Buckius RO. A consistent hydrodynamic boundary condition for the lattice Boltzmann method. Phys Fluids 1995;7:203–9.

[111] Inamuro T, Yoshino M, Ogino F. A non-slip boundary condition for lattice Boltzmann simulations. Phys Fluids 1995;7:2928–30.

[112] Maier RS, Bernard RS, Grunau DW. Boundary conditions for the lattice Boltzmann methods. Phys Fluids 1996;8:1788–801.

[113] Chen S, Martínez D, Mei R. On boundary conditions in lattice Boltzmann method. Phys Fluids 1996;8:2527–36.

[114] Zou Q, He X. On pressure and velocity boundary conditions for the lattice Boltzmann BGK model. Phys Fluids 1997;9:1591–8.

[115] He X, Zou Q, Luo L-S, Dembo M. Analytic solutions and analysis on non-slip boundary condition for the lattice Boltzmann BGK model. J Stat Phys 1997;87:115–36.

[116] Yu D. Viscous flow computations with the lattice Boltzmann equation method. PhD dissertation, University of Florida, 2002.

[117] Grunau DW. Lattice methods for modeling hydrodynamics. PhD dissertation, Colorado State University, 1993.

[118] Skordos PA. Initial and boundary conditions for the lattice Boltzmann method. Phys Rev E 1992;48:4823–42.

[119] He X, Luo L-S. Lattice Boltzmann model for the incompressible Navier–Stokes equation. J Stat Phys 1997;88:927–44.

[120] d'Humières D, Ginzburg I, Krafczyk M, Lallemand P, Luo L-S. Multiple-relaxation-time lattice Boltzmann models in three dimensions. Philos Trans R Soc London A 2002;360:437–51.

[121] Eggels JGM, Sommers JA. Numerical simulation of free convective flow using the lattice-Boltzmann scheme. Int J Heat Fluid Flow 1996;16:357–64.

[122] Shan X. Simulation of Rayleigh–Benard convection using a lattice Boltzmann method. Phys Rev E 1997;55:2780–8.

[123] Succi S, Bella G, Papetti F. Lattice kinetic theory for numerical combustion. J Sci Comput 1997;12:395–408.

[124] Yan G, Chen Y, Hu S. Simple lattice Boltzmann model for simulating flows with shock wave. Phys Rev E 1999;59:454–9.

[125] Hinton FL, Rosenbluth MN, Wong SK, Lin-Liu YR, Miller RL. Modified lattice Boltzmann method for compressible fluid simulations. Phys Rev E 2001;63:061212.

[126] Shi W, Shyy W, Mei R. Finite-difference-based lattice Boltzmann method for inviscid compressible flows. Numer Heat Transfer 2001;B40:1–20.

[127] Huang J, Xu F, Vallieres M, Feng DH, Qian YH, Fryxell B, Strayer MR. A thermal LBGK model for large density and temperature difference. Int J Mod Phys C 1997;8:827–41.

[128] Renda A, Bella G, Succi S, Karlin IV. Thermohydrodynamic lattice BGK schemes with non-perturbative equilibria. Europhys Lett 1998;41:279–83.

[129] Sun C. Simulations of compressible flows with strong shocks by an adaptive lattice Boltzmann model. J Comput Phys 2000;161:70–84.

[130] Mason RJ. A multi-speed compressible lattice-Boltzmann model. J Stat Phys 2002;107:385–400.

[131] Alexander FJ, Chen S, Sterling JD. Lattice Boltzmann thermohydrodynamics. Phys Rev E 1993;47:R2249–52.

[132] Qian YH. Simulating thermohydrodynamics with lattice BGK models. J Sci Comput 1993;8:231–42.

[133] McNamara G, Alder BJ. Analysis of the lattice Boltzmann treatment of hydrodynamics. Physica A 1993;194: 218–28.

[134] McNamara G, Garcia A, Alder BJ. Stabilization of thermal lattice Boltzmann models. J Stat Phys 1995;81: 395–408.

[135] McNamara G, Garcia A, Alder BJ. A hydrodynamically correct thermal lattice Boltzmann model. J Stat Phys 1997;87:1111–21.

[136] He X, Chen S, Doolen GD. A novel thermal model for the lattice Boltzmann method in incompressible limit. J Comput Phys 1998;146:282–300.

[137] Palmer BJ, Rector DR. Lattice Boltzmann algorithm for simulating thermal flow in compressible fluids. J Comput Phys 2000;161:1–19.

[138] Ihle T, Kroll DM. Thermal lattice-Boltzmann method for non-ideal gases with potential energy. Computer Phys Comm 2000;129:1–12.

[139] Inamuro T. A lattice kinetic scheme for incompressible viscous flows with heat transfer. Philos Trans R Soc London A 2002;360:477–84.

[140] Pavlo P, Vahala G, Vahala L, Soe M. Linear stability analysis of thermo-lattice Boltzmann models. J Comput Phys 1998;139:79–91.

[141] Pavlo P, Vahala G, Vahala L. Preliminary results in the use of energy-dependent octagonal lattices for thermal lattice Boltzmann simulations. J Stat Phys 2002;107: 499–519.

[142] Filippova O, Hänel D. A novel lattice BGK approach for low mach number combustion. J Comput Phys 2002;158:139–60.

[143] Nadiga BT. An Euler solver based on locally adaptive discrete velocities. J Stat Phys 1995;81:129–46.

[144] Lallemand P, Luo L-S. Theory of the lattice Boltzmann method: acoustic and thermal properties in two and three dimensions. Phys Rev E 2002, submitted for publication.

[145] Lallemand P, Luo L-S. Hybrid finite-difference thermal lattice Boltzmann equation. Int J Mod Phys B 2003;17: 41–7.

[146] Mezrhab A, Bouzidi M, Lallemand P. Hybrid lattice-Boltzmann finite-difference simulation of convective flows. Comput Fluids 2002, to appear.

[147] Luo L-S. Unified theory of the lattice Boltzmann models for nonideal gases. Phys Rev Lett 1998;81:1618–21.

[148] Luo L-S. Theory of the lattice Boltzmann method: lattice Boltzmann models for nonideal gases. Phys Rev E 2000;62:4982–96.

[149] Luo L-S, Girimaji SS. Lattice Boltzmann model for binary mixtures. Phys Rev E 2002;66:035301.

[150] Luo L-S, Girimaji SS. Theory of the lattice Boltzmann method: Two-Huid model for binary mixtures. Phys Rev E 2003;67:036302.

[151] Sankaranarayanan K, Shan X, Devrekidis IG, Sundaresan S. Analysis of drag and virtual mass forces in bubbly suspensions using an implicit formulation of the lattice Boltzmann method. J Fluid Mech 2002;452:61–96.

[152] Sankaranarayanan K, Kevrekidis IG, Sundaresan S, Lu J, Tryggvason G. A comparative study of lattice Boltzmann and front-tracking finite-difference methods for bubble simulations. Int J Multiphase Flow 2003;29: 109–16.

[153] Ahlrichs P, Dunweg B. Lattice-Boltzmann simulation of polymer-solvent systems. Int J Mod Phys C 1998;9: 1429–38.

[154] Ahlrichs P, Dunweg B. Simulation of a single polymer chain in solution by combining lattice Boltzmann and molecular dynamics. J Chem Phys 1999;111:8225–39.

[155] Ahlrichs P, Everaers R, Dunweg B. Screening of hydrodynamic interactions in semi-dilute polymer solutions: a computer simulation study. Phys Rev E 2002;64: 040501.

[156] Schelkle M, Frohn A. Three-dimensional lattice Boltzmann simulations of binary collisions between equal droplets. J Aerosal Sci 1995;26:S145–6.

[157] Frohn A, Roth N. Dynamics of droplets. Berlin: Springer, 2000.

[158] Sehgal BR, Nourgaliev RR, Dinh TN. Numerical simulation of droplet deformation and break-up by lattice-Boltzmann method. Prog Nucl Energy 1999;34: 471–88.

[159] Xi HW, Duncan C. Lattice Boltzmann simulations of three-dimensional single droplet deformation and breakup under simple shear flow. Phys Rev E 1999;59: 3022–6.

[160] Kang QJ, Zhang DX, Chen SY. Displacement of a two-dimensional immiscible droplet in a channel. Phys Fluids 2002;12:3203–14.

[161] van Kats FM, Egberts PJP. Spreading dynamics modeled by lattice-Boltzmann techniques. J Colloid Interface Sci 1998;205:166–77.

[162] Raiskinmaki P, Koponen A, Merikoski J, Timonen J. Spreading dynamics of three dimensional droplets by the lattice-Boltzmann method. Comp Mater Sci 2000;18: 7–12.

[163] Ginzburg I, Steiner K. Lattice Boltzmann model for free-surface flow and its application to filling process in casting. (Also ITWM Report (34)-2002, (available at http://www.itwm.fhg.de). J Comput Phys 2003;185: 61–99.

[164] He X, Chen SY, Zhang RY. A lattice Boltzmann scheme for incompressible multiphase flow and its application in simulation of Rayleigh–Taylor instability. J Comput Phys 1999;152:642–63.

[165] Nie X, Qian YH, Doolen GD, Chen S. Lattice Boltzmann simulation of the two-dimensional Rayleigh-Taylor instability. Phys Rev E 1998;58:6861–4.

[166] Clark TT. A numerical study of the statistics of a two-dimensional Rayleigh–Taylor mixing layer. Los Alamos National Laboratory Unclassified Report LA-UR-01-3875, Phys Fluids 2001, also submitted for publication.

[167] Gunstensen AK, Rothman DH. Lattice-Boltzmann studies of immiscible 2-phase flow through porous-media. J Geophys Res-Solid Earth 1993;98:6431–41.

[168] Ferréol B, Rothman DH. Lattice-Boltzmann simulations of flow-through Fontainebleau sandstone. Transp Porous Media 1995;20:3–20.

[169] Hill RJ, Koch DL, Ladd AJC. Moderate-Reynolds-number flows in ordered and random arrays of spheres. J Fluid Mech 2001;448:243–78.

[170] Angelopoulos AD, Paunov VN, Burganos VN, Payatakes AC. Lattice Boltzmann simulation of nonideal vapor–liquid flow in porous media. Phys Rev E 1998;57:3237–45.

[171] Hazlett RD, Chen SY, Soll WE. Wettability and rate effects on immiscible displacement: lattice Boltzmann simulation in microtomographic images of reservoir rocks. J Pet Sci Eng 1998;20:167–75.

[172] Spaid MAA, Phelan FR. Modeling void formation dynamics in fibrous porous media with the lattice Boltzmann method. Compos Part A-Appl Sci Manuf 1998;29:749–55.

[173] Bekri S, Vizika O, Thovert JF, Adler PM. Binary two-phase flow with phase change in porous media. Int J Multiph Flow 2001;27:477–526.

[174] Mantle MD, Sederman AJ, Gladden LF. Single- and two-phase flow in fixed-bed reactors: MRI flow visualisation and lattice-Boltzmann simulations. Chem Eng Sci 2001;56:523–9.

[175] Tölke J, Krafczyk M, Schulz M, Rank E. Lattice Boltzmann simulations of binary fluid flow through porous media. Philos Trans R Soc London A 2002;360:535–45.

[176] Ginzburg I, d'Humieres D. Local second-order boundary methods for lattice Boltzmann models. J Stat Phys 1996;84:927–71.

[177] Lallemand P, Luo L-S. Lattice Boltzmann method for moving boundaries. J Comput Phys 2003;184:406–21.

[178] d'Humieres D, Ginzburg I. Multi-reflection boundary conditions for lattice Boltzmann models. ITWM Report (38)-2002 (available at http://www.itwm.fhg.de/).

[179] Verberg R, Ladd AJC. Lattice Boltzmann model with sub-grid-scale boundary conditions. Phys Rev Lett 2000;84:2148–51.

[180] Breuer M, Bernsdorf J, Zeiser T, Durst F. Accurate computations of the laminar flow past a square cylinder based on two different methods: lattice-Boltzmann and finite volume. Int J Heat Fluid Flows 2000;21:186–96.

[181] d'Humieres D, Bouzidi M, Lallemand P. Thirteen-velocity three-dimensional lattice Boltzmann model. Phys Rev E 2001;63:066702.

[182] Junk M, Klar A. Discretizations for the incompressible Navier–Stokes equations based on the lattice-Boltzmann method. SIAM J Sci Comp 2000;22:1–19.

[183] Junk M. A finite difference interpretation of the lattice Boltzmann method. Numer Methods Partial Differential Equations 2002;17:383–402.

[184] Junk M, Klar A, Luo L-S. Theory of the lattice Boltzmann method: mathematical analysis of the lattice Boltzmann equation. J Comput Phys 2002, submitted for publication.

[185] Martínez DO, Matthaeus WH, Chen S, Montgomery DC. Comparison of spectral method and lattice Boltzmann simulations of two-dimensional hydrodynamics. Phys Fluids 1994;6:1285–98.

[186] Trevino C, Higuera F. Lattice Boltzmann and spectral simulations of non-linear stability of Kolmogorov flows. Rev Mex Fis 1994;40:878–90.

[187] Vergassola M, Benzi R, Succi S. On the hydrodynamic behavior of the lattice Boltzmann-equation. Europhys Lett 1990;13:411–6.

[188] Chen S, Wang Z, Shan XW, Doolen GD. Lattice Boltzmann computational fluid dynamics in three dimensions. J Stat Phys 1992;68:379–400.

[189] Benzi R, Struglia MV, Tripiccione R. Extended self-similarity in numerical simulations of three-dimensional anisotropic turbulence. Phys Rev E 1996;53:R5565–8.

[190] Luo L-S, Wang L-P, Qi DW. Applications of the lattice Boltzmann method to complex and turbulent flows. In: Breuer M, Durst F, Zenger C, editors. High Performance Scientific and Engineering Computing. Proceedings of the 3rd International FORTWIHR Conference on HPSEC, Erlangen, March 12–14, 2001. Lecture Notes in Computational Science and Engineering, vol. 21. Berlin: Springer, 2002. pp. 123–30.

[191] Eggels JMG. Direct and large-eddy simulation of turbulent fluid flow using the lattice-Boltzmann scheme. Int J Heat Fluid Flow 1996;17:307–23.

[192] Hou S, Sterling J, Chen S, Doolen GD. A lattice Boltzmann subgrid model for high Reynolds number flows. In: Lawniczak AT, Kapral R, editors. Pattern formation and lattice gas automata. Fields Institute Communications 6, Providence, RI: AMS, 1996. p. 151–66.

[193] Derksen J, Van den Akker HEA. Parallel simulation of turbulent fluid flow in a mixing tank. LNCS 1998;1401:96–104.

[194] Derksen J, Van den Akker HEA. Large eddy simulations on the flow driven by a Rushton turbine. AICHE J 1999;45:209–21.

[195] Derksen J, Van den Akker HEA. Simulation of vortex core precession in a reverse-flow cyclone. AICHE J 2000;46:1317–31.

[196] Krafczyk M. Gitter–Boltzmann–Methoden: Von der Theorie zur Anwendung. Habilitation Thesis, Techische Universitat Munchen, Munchen, 2001.

[197] Lu ZY, Liao Y, Qian DY, McLaughlin JB, Derksen JJ, Kontomaris K. Large eddy simulations of a stirred tank using the lattice Boltzmann method on a nonuniform grid. J Comput Phys 2002;181:675–704.

[198] Krafczyk M, Tölke J, Luo L-S. Large-eddy simulations with a multiple-relaxation-time LBE model. Int J Mod Phys B 2003;17:33–9.

[199] Smagorinsky J. General circulation experiments with the primitive equations. I. The basic experiment. Mon Weather Rev 1963;91:99–164.

[200] Martinuzzi R, Tropea C. The flow around surface-mounted, prismatic obstacles placed in a fully developed channel flow. ASME J Fluids Eng 1993;115:85–92.

[201] Rodi W, Ferziger JH, Breuer M, Pourquie M. Status of large-eddy simulation: results of a workshop. ASME J Fluids Eng 1997;119:248–62.

[202] Karniadakis EmG, Beskok A. Micro flows. New York: Springer, 2002.

[203] Kuksenok O, Yeomans JM, Balazs AC. Creating localized mixing stations within micro fluidic channels. Langmuir 2001;17(23):7186–90.

[204] Lim CY, Shu C, Niu XD, Chew YT. Application of lattice Boltzmann method to simulate microchannel flows. Phys Fluids 2002;14(7):2299–308.

[205] Thamida SK, Chang HC. Nonlinear electrokinetic ejection and entrainment due to polarization at nearly insulated wedges. Phys Fluids 2002;14(12):4315–28.

[206] Kuksenok O, Yeomans JM, Balazs AC. Using patterned substrates to promote mixing in microchannels. Phys Rev E 2002;65(3):031502.

[207] Berger MJ, Oliger J. Adaptive mesh refinement for hyperbolic partial differential equations. J Comput Phys 1984;53:484–512.

[208] Baker TJ. Mesh adaptation strategies for problems in fluid dynamics. Finite Elements Anal Design 1997;25: 243–73.

[209] Steinthorsen E, Modiano E, Crutchfield WY, Bell LB, Colella P. An adaptive semi-implicit scheme for simulations of unsteady viscous compressible flow. In: AIAA Paper 95-1727-CP, Proceedings of the 12th AIAA CFD Conference, 1995.